Modeling of Multipoint Fuel Injection for the Large Eddy Simulation of Aeronautical Combustion Chambers

Carlos G. Guillamón

Contents

Acknowledgements

Nomenclature

Abstract

Résumé

List of Figures

List of Tables

Chapter 1
Introduction

1.1 General context

In the 20th century, the field of aeronautics has experimented a hectic growth since World War I (1914 - 1919), when airplanes played a fundamental role in the aerial battles. The advances in military aviation led to the apparition of the first airlines and the birth of commercial aviation after the war. It was not, however, until World War II (1939 - 1945) that the biggest progresses were made: technological improvements resulted in larger, more efficient aircrafts that were used for surveillance, in air battles or for bombing purposes. After this period, airplanes used during the war were recycled with civil purposes to transport cargo and passengers. This supposed the beginning of a new era for commercial aviation that has not stopped to grow until nowadays, where air transportation is an essential activity in today's society.

The increasing relevance of commercial aviation has been possible due to advances in aeronautical technologies, from structures and control systems to propulsion systems. In the case of the latter, the birth of the jet engine in the 1930s supposed a milestone that marked the transition from propelled airplanes working with internal combustion engines to faster ones powered by gas turbines. Improvements in propulsion technologies have led to bigger, more efficient engines which can produce more power in order to drive bigger airplanes faster during longer times, hence covering longer distances.

However, despite today's propulsion technologies being more efficient than those from its origins, they are not extent of producing emissions. Species generated during the combustion process in gas turbines include CO_2, a greenhouse gas contributing to global warming, and CO and NO_x, considered as pollutant emissions. In this respect, the increasing demand of commercial transportation and a rising general concern about the effects of climate change, have placed the need of reducing emissions, as well as noise, as a major constraint for the development of aviation in the decades to come. The Advisory Council of Aeronautic Research in Europe (ACARE) has settled the goal to reduce the emissions per passenger/kilometre of CO_2 by 75 % and of NO_x by 90 % for the year 2050 with respect to the levels of 2000 (**?**).

Emissions of NO_x are a big concern due to their harmful effect in health and environment (e.g. it is one of the main species producing acid rain). The evolution of aeronautical engines in the last decades have led to higher combustion temperatures and larger Overall Pressure Ratios (OPR), which help to reduce fuel consumption but increase the production of NO_x. Engine manufacturers have worked on mitigating this increasing trend, as shown by the evolution of NO_x emissions with OPR for several generations of engines in Figure 1.1. It is shown how certified engines have succeeded in reducing emissions below the ICAO-CAEP regulatory limits. Nevertheless, the NO_x are still expected to grow due to the expanding aerial traffic demand. Figure 1.2 displays the forecasts for several traffic scenarios, where it is shown the potential effect of technology advances in the emissions at 2040 (lower bounds) with respect to the case where current technologies (of year 2017) would be used (upper bounds). Therefore, in order to maintain the emissions below a certain level and hence accomplish the ACARE goals, substantial efforts need to be done. One way of achieving this is by controlling and improving the combustion process, since it is known that NO_x are produced at high temperatures. For this purpose, the aeronautical community is working towards new combustion chambers and injection processes aiming at creating **lean combustion**.
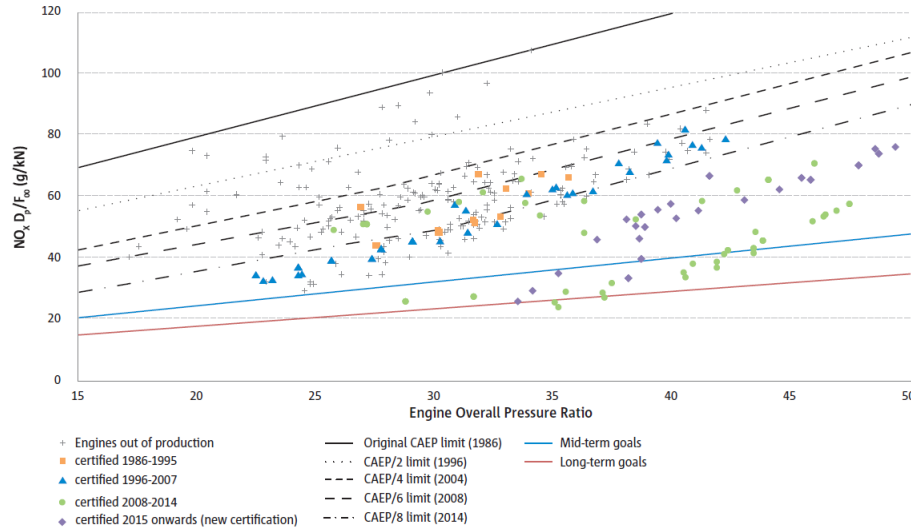
Figure 1.1: Evolution of NO_x emissions with several generations of aircraft engines. Source: (**?**)
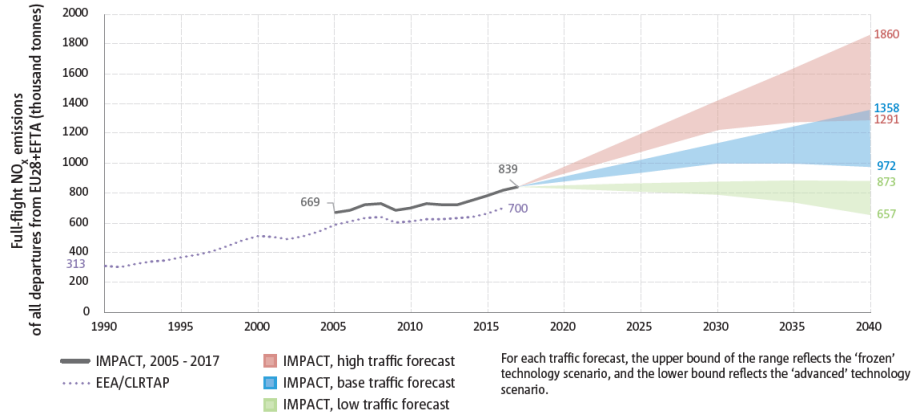
Figure 1.2: NO_x emission forecasts from 2017 to 2040. Source: (**?**)

1.2 Lean combustion in aeronautical gas turbines

With the objective of reducing NO_x emissions in aeronautical combustion chambers, the community has worked towards the implementation of concepts aiming at producing lean combustion (low-NO_x systems). The motivation under this regime is shown in Figure 1.3: at lean regimes (i.e. with an excess of air), the flame temperature is lower and, consequently, formation of NO_x is reduced. At the same time, emissions of CO, hydrocarbons (HC) and soot are also diminished at this regime (provided that the air excess is not too high, or the emissions will start to grow again). On the contrary, operating at lean regimes will make the system more prone to thermoacoustic instabilities and will place it closer to the the limit of lean blow-out (LBO), hindering ignition and relight capabilities.

In order to foster lean combustion, low-NO_x concepts introduce an excess of air at the vicinity of the injector: around 70 % of air is introduced in the combustion chamber at this location (primary zone), while the rest is used further downstream for effusion cooling. Compared to conventional combustors, where around 30 % of air is injected in the primary zone and the rest is introduced further downstream through dilution holes, this allows to reduce the length of the combustion chamber and hence the residence time of combustion, directly linked to NO_x formation (**?**).

One of the first concept aiming at reducing NO_x emissions is the Rich-burn/Quick-quench/Lean-burn (RQL) combustor (**?**). In RQL systems, combustion takes place firstly in a rich primary zone where the

For making low-NO_x systems possible and alleviating their drawbacks, new concepts
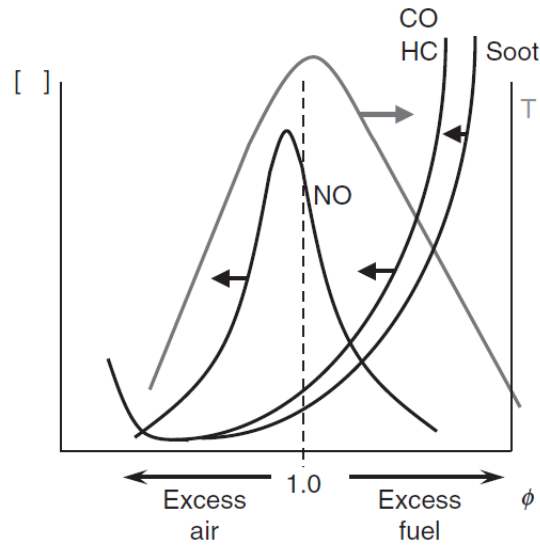
Figure 1.3: Temperature and species concentration variation with stoichiometric ratio in combustion chambers. Source: **?**.
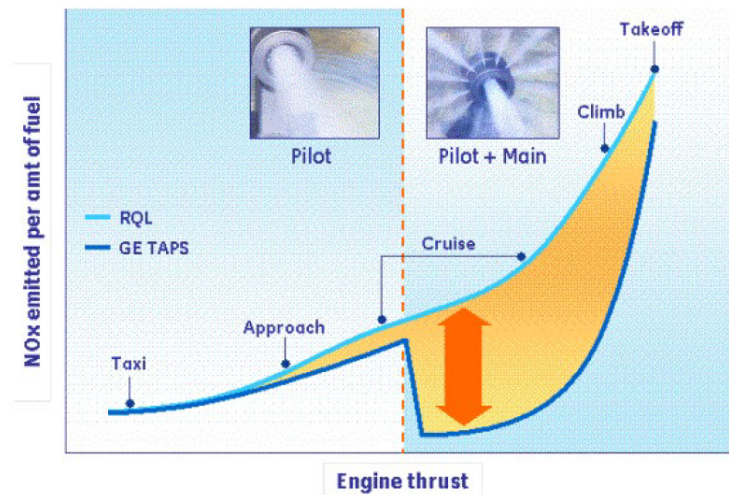
Figure 1.4: Source: **?**.

1.3 Fuel injection technology

Atomization process

Explain two-phase flows phenomenology (injection + atomization) here.
Explain airblast, hollow-cone, jicf.

1.4 Objective and thesis outline

secondary breakup

primary breakup

dense regime

dilute regime

intermediate regime

$\ell / \Delta x > 1$
$\Theta = O(1)$

$\ell / \Delta x < 1$
$\Theta < 1$

$\ell / \Delta x \ll 1$
$\Theta \ll 1$

Δx : grid resolution
Θ : liquid volume fraction
ℓ : characterisitic liquid length scale
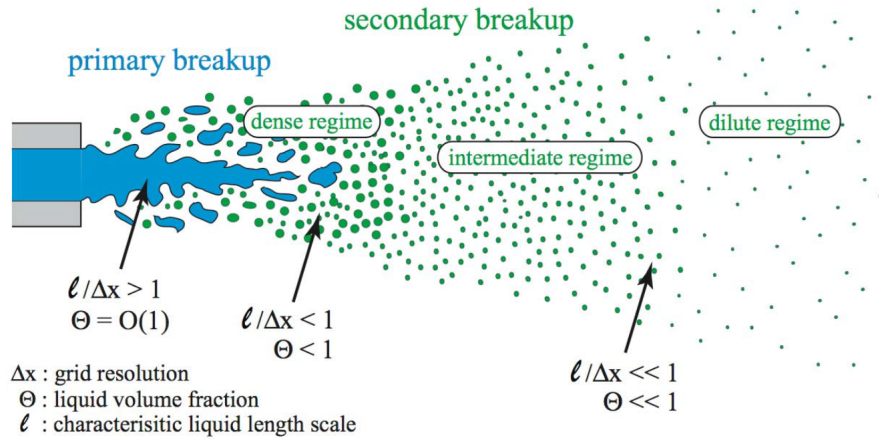
Figure 1.5: Atomization breakup regimes (**?**)

Part I

Numerical approaches to model injection systems

Chapter 2

Numerical methods to simulate resolved atomization

2.1 Introduction

MAKE LINK WITH FINAL PART OF INTRODUCTION WHEN IT IS DONE

Resolution of two-phase flows requires a suitable description of each phase and a careful treatment of the liquid-gas interface. From a numerical point of view, the multi-scale nature of atomization makes it impossible to use the same methods for resolving atomization accurately and for transporting a developed spray, since the characteristic length scales differ by several orders of magnitude. Consequently, different numerical methodologies must be chosen according to the targeted problem. Furthermore, if multi-physical phenomena, such as evaporation or combustion, are present, the range of possible models to be applied becomes even narrower.

The first step to choose a proper methodology is to identify the type of regime to solve. One possible classification of two-phase regimes can be done depending on the distribution and topology of the interface. In this respect, one can distinguish between separate and disperse phase (**?**):

- **Separate phase** flows, also known as dense regime, present a clear definition of the interface and both liquid and gaseous phases can be easily identified (Figure 2.1 left). In such cases, the liquid volume fraction is large and the liquid structures are of the same order, or larger, than the cell size, so the atomization dynamics can be captured by the mesh. Within engines, separate phase is found during primary breakup, as shown by the blue regions of Fig. 1.5. Numerical methods devoted to resolve separate phase regimes are tackled in this chapter (§2.3). Generally, these methods are restricted to non-reactive problems and the multi-physics coupling with evaporation and combustion is not possible.

- **Dispersed phase** regime is found when the liquid volume fraction is small and the liquid structures cannot be capture by the main grid. The liquid phase is composed by individual liquid particles (usually called droplets) whose high number and small size hinders the tracking of the interface (Figure 2.1 right). Droplets are surrounded by the gaseous phase, also called **carrier phase**. A developed spray produced as a consequence of secondary atomization is an example of dispersed phase systems, illustrated by the intermediate and dilute regimes of Figure 1.5. The same numerical methods used for the separate phase regime cannot be applied, since the characteristic scales are much smaller and the grid resolution required yields the computations unaffordable due to their high cost. Numerical formalisms targeting dispersed phase flows are discussed in Chapter 3. These methods do not resolve atomization as accurately as the ones employed for separate phases, but present the possibility to integrate evaporation and combustion.

An insightful classification of existing numerical methods for two-phase flows is shown in Figure 2.2. Methods aiming at solving disperse-phase flows use often a two-fluid formulation, since the description of each phase is often done with separate equations. On the other hand, methods addressing separate phases are based on a one-fluid formulation, since basically the same governing equations are solved but distinguishing
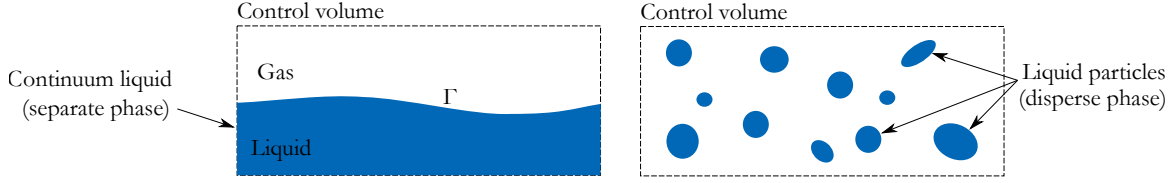
Figure 2.1: Two-phase systems classification. *Left*: separate flow, where both phases are easily distinguished and the interface Γ can easily be tracked. *Right*: dispersed phase flow, where individual fluid particles (disperse phase) are surrounded by the gas (carrier phase). In such systems, the interface can hardly be tracked due to the higher surface-to-volume ratio.

between phases via their different physical properties. This requires a specific treatment of the interface and the jump conditions in pressure due to surface tension, which each method will handle differently.

This chapter gives an overview on the state-of-the-art in numerical methods applicable to resolve separate phase regimes. Section 2.2 introduces the governing equations of non-reactive two phase flows, beginning by introducing the Reynolds Transport Theorem and applying it to obtain mass and momentum conservation laws. Section 2.3 presents the numerical methodologies reviewed: diffuse interface, front-tracking, Volume of Fluid (VOF), and Accurate Conservative Level-Set coupled with Ghost-Fluid Method (ACLS/GMF). The last one is the methodology used in this thesis for performing resolved simulation atomizations in Chapter 5.
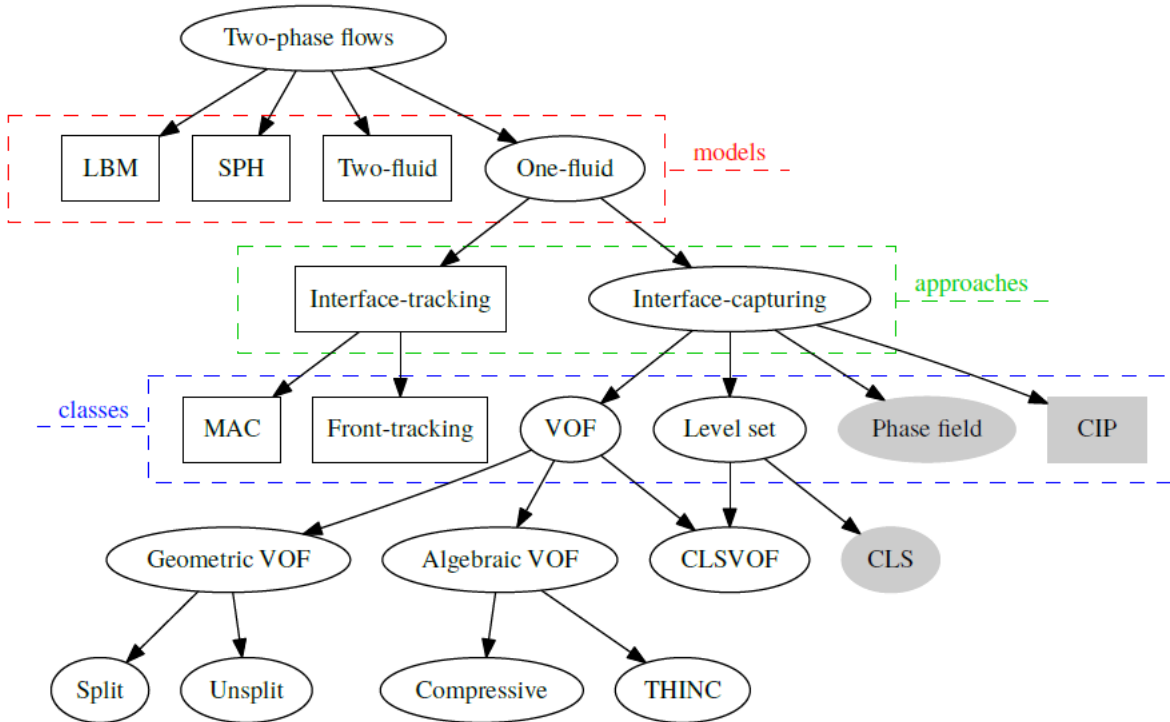
Figure 2.2: Numerical methods to simulate two-phase flows. Ellipses denote interface-capturing methods. Sharp-interface methods are denoted by a white background, while the grey one indicates diffuse-interface methods. Source: **?**

2.2 Governing equations

2.2.1 Reynolds transport theorem

General form

The starting point for deriving all the conservation equations is the Reynolds transport theorem (RTT). Let's consider a control volume Ω bounded by a control surface $\partial\Omega$. Let's also consider a control mass Ω_m which moves with time to enclose the same amount of mass. This control mass coincides at some time instant with the control volume. The RTT relates the variation of a property $\phi = \phi(\boldsymbol{x}, t)$ in the control mass with its variation in the control volume. In its most general form, it can be expressed as follows (**?**):

$$\frac{d}{dt}\int_{\Omega_m}\phi dV = \frac{d}{dt}\int_\Omega \phi dV + \int_{\partial\Omega}\phi\left(\boldsymbol{u} - \boldsymbol{u_c}\right)\cdot\boldsymbol{n}dS \tag{2.1}$$

where $\boldsymbol{u}$ is the flow velocity at the boundaries, $\boldsymbol{u_c}$ is the velocity of the control surface and $\boldsymbol{n}$ is the normal unit vector pointing outwards the surface of the control volume. Bold symbols indicate vectorial quantities.

The first term in the right hand side can be expanded by applying Leibniz's integral rule to a domain with moving boundaries. Following the introduced notation, Leibniz's rule takes the following shape:

$$\frac{d}{dt}\int_\Omega \phi dV = \int_\Omega \frac{\partial\phi}{\partial t}dV + \int_{\partial\Omega}\phi\left(\boldsymbol{u_c}\cdot\boldsymbol{n}\right)dS \tag{2.2}$$

The latter equation can also be seen as another expression for the RTT particularised for a moving control volume. Introducing it into (2.1) yields:

$$\boxed{\frac{d}{dt}\int_{\Omega_m}\phi dV = \int_\Omega \frac{\partial\phi}{\partial t}dV + \int_{\partial\Omega}\phi\left(\boldsymbol{u}\cdot\boldsymbol{n}\right)dS} \tag{2.3}$$

This formulation of the relates the lagrangian formulation of a system (left hand side, corresponding to the control mass) with the eulerian formulation (right hand side, corresponding to the control volume).

In this document all the control volumes selected for performing balances will be fixed in space, so their boundaries not move. Consequently, $\boldsymbol{u_c} = 0$ and hence Eq. (2.2) becomes $\frac{d}{dt}\int_\Omega \phi dV = \int_\Omega \partial\phi/\partial t\, dV$.

Application to two-phase flows

In the particular case of two-phase flows systems comprising gas and liquid phases, denoted respectively by the subscripts g and l, the domain can be decomposed into two subdomains Ω_g and Ω_l. The addition of these two subdomains will make the total domain Ω:

$$\Omega = \Omega_\mathrm{g} \cup \Omega_\mathrm{l} \tag{2.4}$$

The RTT must hold for each subdomain, so Eq. (2.3) can be applied to each phase separately

$$\frac{d}{dt}\int_{\Omega_{m_\mathrm{g}}}\phi\, dV = \int_{\Omega_\mathrm{g}}\frac{\partial\phi}{\partial t}\, dV + \int_{\partial\Omega_\mathrm{g}}\phi\left(\boldsymbol{u}\cdot\boldsymbol{n}\right)dS \tag{2.5a}$$

$$\frac{d}{dt}\int_{\Omega_{m_\mathrm{l}}}\phi\, dV = \int_{\Omega_\mathrm{l}}\frac{\partial\phi}{\partial t}\, dV + \int_{\partial\Omega_\mathrm{l}}\phi\left(\boldsymbol{u}\cdot\boldsymbol{n}\right)dS \tag{2.5b}$$

The surface integral in the right hand side can be decomposed in two different integrals by considering a common boundary shared by both subdomains: the liquid-gas interface Γ. This interface can be modified with time. Hence, the control boundary $\partial\Omega$ can be expressed as the addition of the following two subdomains:

$$\partial\Omega = (\partial\Omega_\mathrm{g}\backslash\Gamma) \cup (\partial\Omega_\mathrm{l}\backslash\Gamma) \tag{2.6}$$

So the RTT for separate phases can be extended as follows:

$$\frac{d}{dt}\int_{\Omega_{m_g}}\phi\,dV = \int_{\Omega_g}\frac{\partial\phi}{\partial t}\,dV + \int_{\partial\Omega_g\backslash\Gamma}\phi\,(\boldsymbol{u}\cdot\boldsymbol{n})\,dS + \int_{\Gamma}\phi_g\,(\boldsymbol{u}_\Gamma\cdot\boldsymbol{n}_{\Gamma g})\,dS \tag{2.7a}$$

$$\frac{d}{dt}\int_{\Omega_{m_l}}\phi\,dV = \int_{\Omega_l}\frac{\partial\phi}{\partial t}\,dV + \int_{\partial\Omega_l\backslash\Gamma}\phi\,(\boldsymbol{u}\cdot\boldsymbol{n})\,dS + \int_{\Gamma}\phi_l\,(\boldsymbol{u}_\Gamma\cdot\boldsymbol{n}_{\Gamma l})\,dS \tag{2.7b}$$

where $\boldsymbol{u}_\Gamma$ is the velocity at the interface and $\boldsymbol{n}_\Gamma$ is the vector normal to the interface pointing outwards its corresponding phase. As the interface is the same but the outward direction is opposed for each phase, an interface normal vector pointing to the liquid phase can be defined:

$$\boldsymbol{n}_\Gamma = \boldsymbol{n}_{\Gamma l} = -\boldsymbol{n}_{\Gamma g} \tag{2.8}$$

Hence, the RTT for each separate phase can be reformulated as:

$$\frac{d}{dt}\int_{\Omega_{m_g}}\phi\,dV = \int_{\Omega_g}\frac{\partial\phi}{\partial t}\,dV + \int_{\partial\Omega_g\backslash\Gamma}\phi\,(\boldsymbol{u}\cdot\boldsymbol{n})\,dS - \int_{\Gamma}\phi_g\,(\boldsymbol{u}_\Gamma\cdot\boldsymbol{n}_\Gamma)\,dS \tag{2.9a}$$

$$\frac{d}{dt}\int_{\Omega_{m_l}}\phi\,dV = \int_{\Omega_l}\frac{\partial\phi}{\partial t}\,dV + \int_{\partial\Omega_l\backslash\Gamma}\phi\,(\boldsymbol{u}\cdot\boldsymbol{n})\,dS + \int_{\Gamma}\phi_l\,(\boldsymbol{u}_\Gamma\cdot\boldsymbol{n}_\Gamma)\,dS \tag{2.9b}$$

Finally, a general shape for the RTT in two-phase flows can be obtained by adding Equations (2.9) and applying (2.4) and (2.6):

$$\frac{d}{dt}\int_{\Omega_m}\phi\,dV = \int_{\Omega}\frac{\partial\phi}{\partial t}\,dV + \int_{\partial\Omega}\phi\,(\boldsymbol{u}\cdot\boldsymbol{n})\,dS + \int_{\Gamma}(\phi_l - \phi_g)\,(\boldsymbol{u}_\Gamma\cdot\boldsymbol{n}_\Gamma)\,dS \tag{2.10}$$

2.2.2 Mass conservation

General forms

The mass conservation equation for a fluid system is obtained by substituting $\phi = \rho$ in Eq. (2.3):

$$\frac{d}{dt}\int_{\Omega_m}\rho\,dV = \int_{\Omega}\frac{\partial\rho}{\partial t}\,dV + \int_{\partial\Omega}\rho\boldsymbol{u}\cdot\boldsymbol{n}\,dS \tag{2.11}$$

By definition, the control mass is a region of the fluid flow whose mass does not change. Hence, the left hand side of the previous expression is 0 and the **mass conservation in integral form**, or **weak form of mass conservation**, is expressed as follows:

$$\boxed{\int_{\Omega}\frac{\partial\rho}{\partial t}\,dV + \int_{\partial\Omega}\rho\boldsymbol{u}\cdot\boldsymbol{n}\,dS = 0} \tag{2.12}$$

The Gauss theorem can be applied to a vectorial field $\boldsymbol{f}$ to transform a surface integral into a volume integral:

$$\int_{\partial\Omega}\boldsymbol{f}\cdot\boldsymbol{n}\,dS = \int_{\Omega}\nabla\boldsymbol{f}\,dV \tag{2.13}$$

Applying this theorem considering $\boldsymbol{f} = \rho\boldsymbol{u}$ and substituting into (2.12) yields the general expression for **mass conservation in differential form** or **strong form of mass conservation**:

$$\boxed{\frac{\partial\rho}{\partial t} + \nabla\,(\rho\boldsymbol{u}) = 0} \tag{2.14}$$

This equation is also known as the **continuity equation in conservative form**. The **non-conservative** form can be obtained by expanding the left-hand side:

$$\frac{\partial\rho}{\partial t} + \nabla\,(\rho\boldsymbol{u}) = \frac{\partial\rho}{\partial t} + \boldsymbol{u}\cdot\nabla\rho + \rho\nabla\boldsymbol{u} = 0 \quad\rightarrow\quad \frac{d\rho}{dt} + \rho\nabla\boldsymbol{u} = 0 \tag{2.15}$$

where $d/dt = \partial/\partial t + \boldsymbol{u}\cdot\nabla$ is the **material derivative**.

Hereafter, the weak form of mass conservation will be addressed for its application in integral balances.

Global mass conservation in two-phase flows

A global expression for mass conservation can be obtained by substituting $\phi = \rho$ into Eq. (2.10):

$$\frac{d}{dt}\int_{\Omega_m} \rho dV = \int_\Omega \frac{\partial \rho}{\partial t} dV + \int_{\partial\Omega} \rho \boldsymbol{u} \cdot \boldsymbol{n} dS + \int_\Gamma (\rho_l - \rho_g)(\boldsymbol{u}_\Gamma \cdot \boldsymbol{n}_\Gamma) dS \tag{2.16}$$

In conditions where mass exchange takes place, such as the hot environment within combustion chambers, high temperature might produce evaporation of the liquid phase into gaseous phase. In such cases, the left hand side term of the former equation would be a sink term different to zero. However in this work mass exchange is not considered, so this term is zero:

$$\int_\Omega \frac{\partial \rho}{\partial t} dV + \int_{\partial\Omega} \rho \boldsymbol{u} \cdot \boldsymbol{n} dS + \int_\Gamma (\rho_l - \rho_g)(\boldsymbol{u}_\Gamma \cdot \boldsymbol{n}_\Gamma) dS = 0 \tag{2.17}$$

It can be noticed that the first two integrals in this expression correspond to the weak form for mass conservation as given by Eq. (2.12). Hence, this expression is simplified to:

$$\int_\Gamma (\rho_l - \rho_g)(\boldsymbol{u}_\Gamma \cdot \boldsymbol{n}_\Gamma) dS = 0 \tag{2.18}$$

As both ρ_l and ρ_g are always positive, and $\rho_l > \rho_g$ for most known applications (including gas turbines and atmospheric two-phase systems), the only possibility for this expression to hold true is when the dot product is zero:

$$\boxed{\boldsymbol{u}_\Gamma \cdot \boldsymbol{n}_\Gamma = 0} \tag{2.19}$$

which means that the flow velocity normal to the interface must be zero, i.e. there is no liquid or gas crossing the interface.

Mass conservation in separate phases

Two-phase flows must ensure mass conservation for each phase. This can be done by applying the RTT as given by Eqs. (2.9) to the field $\phi = \rho$. However this formulation introduces the need to deal with the liquid-gas interface, which is often changing in time. A more useful formulation can be developed by the strong form given by (2.12) to each phase separately (**?**). For making it properly, it is necessary to introduce before the definition of **volumetric fraction** for a phase k, α_k:

$$\alpha_k = \frac{V_k}{V} \tag{2.20}$$

This magnitude determines the quantity of a given fluid k that is contained in a considered volume V. By definition, it follows that $\sum_{k=1}^{N_{phases}} \alpha_k = 1$. It can be defined for both gas and liquid phases, α_g and α_l, so then $\alpha_g + \alpha_l = 1$.

Once the volumetric fractions for liquid and gas have been defined, the continuity equation (2.14) can be defined for each phase as follows:

$$\frac{\partial \alpha_g \rho_g}{\partial t} + \nabla(\alpha_g \rho_g \boldsymbol{u}_g) = 0 \tag{2.21a}$$

$$\frac{\partial \alpha_l \rho_l}{\partial t} + \nabla(\alpha_l \rho_l \boldsymbol{u}_l) = 0 \tag{2.21b}$$

The integral balance can be obtained by integrating both expressions over a fixed control volume Ω and applying the Gauss theorem to the divergence term:

$$\frac{\partial}{\partial t}\int_\Omega \alpha_g \rho_g dV + \int_{\partial\Omega} \alpha_g \rho_g (\boldsymbol{u}_g \cdot \boldsymbol{n}) dS = 0 \tag{2.22a}$$

$$\frac{\partial}{\partial t}\int_\Omega \alpha_l \rho_l dV + \int_{\partial\Omega} \alpha_l \rho_l (\boldsymbol{u}_l \cdot \boldsymbol{n}) dS = 0 \tag{2.22b}$$

These equations present two components: a transient term and a surface term. The transient term has an effect when the mass of any phase is growing inside the control volume, e.g. at the first instants of fuel injection, when the fuel mass is increasing with time. Once a steady-state has been reached, this term becomes 0. The surface term accounts for the mass fluxes that are entering of leaving the system through its boundaries. From this term, the **mass flow rate** $\dot{m}$ of a flux going though an area A can be defined as:

$$\dot{m} = \int_A \rho \left(\boldsymbol{u} \cdot \boldsymbol{n} \right) dS \tag{2.23}$$

An inspection of this equation reveals a dot product between the velocity vector and the normal vector to the surface. As the normal vector is pointing outwards the control volume, the dot product will be positive in surfaces where both vectors have the same direction, and negative otherwise. Hence, the mass flow rate will be positive in outlets and negative in inlets.

If the transient term in (2.22), which is a source term, is denoted as $\dot{\Omega}_m$, then the mass conservation for separated phases can be written as follows:

$$\dot{\Omega}_{m_\text{g}} + \sum_i \dot{m}_{g_i} = 0 \tag{2.24a}$$

$$\dot{\Omega}_{m_\text{l}} + \sum_j \dot{m}_{l_j} = 0 \tag{2.24b}$$

Considering that inlet fluxes are negative and outlet fluxes are positive, the equations can be rearranged:

$$\dot{\Omega}_{m_\text{g}} = \sum_{i_\text{in}} \dot{m}_{g_i} - \sum_{i_\text{out}} \dot{m}_{g_i} \tag{2.25a}$$

$$\dot{\Omega}_{m_\text{l}} = \sum_{j_\text{in}} \dot{m}_{l_j} - \sum_{j_\text{out}} \dot{m}_{l_j} \tag{2.25b}$$

2.2.3 Momentum conservation

General forms

The momentum conservation equation for a fluid system is obtained by substituting $\phi = \rho \boldsymbol{u}$ in Eq. (2.3):

$$\frac{d}{dt} \int_{\Omega_m} \rho \boldsymbol{u} dV = \int_\Omega \frac{\partial (\rho \boldsymbol{u})}{\partial t} dV + \int_{\partial \Omega} \rho \boldsymbol{u} \left(\boldsymbol{u} \cdot \boldsymbol{n} \right) dS \tag{2.26}$$

The left-hand side term represents the ensemble of forces acting in the control mass. These forces can be separated into volume and surface forces. The volume forces will be denoted by $\boldsymbol{b}$; the surface forces include the pressure p and the viscous stress tensor $\bar{\bar{\boldsymbol{\tau}}}$. With this notation, the **momentum conservation in integral form**, or **weak form of momentum conservation**, is defined as:

$$\int_\Omega \frac{\partial (\rho \boldsymbol{u})}{\partial t} dV + \int_{\partial \Omega} \rho \boldsymbol{u} \left(\boldsymbol{u} \cdot \boldsymbol{n} \right) dS = \int_{\partial \Omega} \left(-p \bar{\bar{\boldsymbol{I}}} + \bar{\bar{\boldsymbol{\tau}}} \right) \boldsymbol{n} dS + \int_\Omega \boldsymbol{b} dV \tag{2.27}$$

where $\bar{\bar{\boldsymbol{I}}}$ is the identity matrix. Applying the Gauss theorem (2.13) with $\boldsymbol{f} = \rho \boldsymbol{u} \boldsymbol{u}$ and operating yields the **momentum conservation in differential form**, or **strong form of momentum conservation**:

$$\frac{\partial (\rho \boldsymbol{u})}{\partial t} + \nabla \left(\rho \boldsymbol{u} \boldsymbol{u} \right) = -\nabla p + \nabla \bar{\bar{\boldsymbol{\tau}}} + \boldsymbol{b} \tag{2.28}$$

This solution is also known as the **conservative form of the momentum equation**. The left-hand side can be further expanded:

$$\frac{\partial (\rho \boldsymbol{u})}{\partial t} + \nabla \left(\rho \boldsymbol{u} \boldsymbol{u} \right) = \boldsymbol{u} \underbrace{\left[\frac{\partial \rho}{\partial t} + \nabla \left(\rho \boldsymbol{u} \right) \right]}_{\substack{\text{Continuity} \\ \text{equation (2.14)}}} + \rho \left[\frac{\partial \boldsymbol{u}}{\partial t} + \boldsymbol{u} \cdot \nabla \boldsymbol{u} \right] = \rho \left(\frac{\partial \boldsymbol{u}}{\partial t} + \boldsymbol{u} \cdot \nabla \boldsymbol{u} \right) = \rho \frac{d\boldsymbol{u}}{dt} \tag{2.29}$$

With this notation, the **non-conservative form** is obtained:

$$\rho \frac{d\boldsymbol{u}}{dt} = -\nabla p + \nabla \overline{\overline{\boldsymbol{\tau}}} + \boldsymbol{b} \tag{2.30}$$

Global momentum conservation in two-phase flows

A global expression for momentum conservation can be obtained by substituting $\phi = \rho \boldsymbol{u}$ into Eq. (2.10):

$$\frac{d}{dt} \int_{\Omega_m} \rho \boldsymbol{u} dV = \int_{\Omega} \frac{\partial \rho \boldsymbol{u}}{\partial t} dV + \int_{\partial \Omega} \rho \boldsymbol{u} \left(\boldsymbol{u} \cdot \boldsymbol{n} \right) dS + \int_{\Gamma} \left(\rho_l \boldsymbol{u}_l - \rho_g \boldsymbol{u}_g \right) \left(\boldsymbol{u}_\Gamma \cdot \boldsymbol{n}_\Gamma \right) dS \tag{2.31}$$

The left-hand side term can be expressed in the same way as in Eq. (2.27) with a slight modification: another addend must be included to account for the interface, as done in §2.2.1. In this way, this term becomes:

$$\frac{d}{dt} \int_{\Omega_m} \rho \boldsymbol{u} dV = \int_{\partial \Omega} \left(-p \overline{\overline{\boldsymbol{I}}} + \overline{\overline{\boldsymbol{\tau}}} \right) \boldsymbol{n} dS + \int_{\Omega} \boldsymbol{b} dV + \int_{\Gamma} \left[-\left(p_l - p_g \right) \overline{\overline{\boldsymbol{I}}} + \left(\overline{\overline{\boldsymbol{\tau}}}_l - \overline{\overline{\boldsymbol{\tau}}}_g \right) + \overline{\overline{\boldsymbol{\tau}}}_\sigma \right] \boldsymbol{n} dS \tag{2.32}$$

In the interface term, a new contribution has been added: surface tension, represented in this equation by the tensor $\overline{\overline{\boldsymbol{\tau}}}_\sigma$. Surface tension only contributes in the interface. These terms can now be introduced in the momentum conservation equation:

$$\int_{\Omega} \frac{\partial \rho \boldsymbol{u}}{\partial t} dV + \int_{\partial \Omega} \rho \boldsymbol{u} \left(\boldsymbol{u} \cdot \boldsymbol{n} \right) dS + \int_{\Gamma} \left(\rho_l \boldsymbol{u}_l - \rho_g \boldsymbol{u}_g \right) \left(\boldsymbol{u}_\Gamma \cdot \boldsymbol{n}_\Gamma \right) dS =$$
$$= \int_{\partial \Omega} \left(-p \overline{\overline{\boldsymbol{I}}} + \overline{\overline{\boldsymbol{\tau}}} \right) \boldsymbol{n} dS + \int_{\Omega} \boldsymbol{b} dV + \int_{\Gamma} \left(-\left(p_l - p_g \right) \overline{\overline{\boldsymbol{I}}} + \left(\overline{\overline{\boldsymbol{\tau}}}_l - \overline{\overline{\boldsymbol{\tau}}}_g \right) + \overline{\overline{\boldsymbol{\tau}}}_\sigma \right) \boldsymbol{n} dS \tag{2.33}$$

Inspecting this equation reveals that the first two terms in both sides make the general integral form of momentum conservation, Eq. (2.27). Therefore, the equation can be simplified:

$$\int_{\Gamma} \left(\rho_l \boldsymbol{u}_l - \rho_g \boldsymbol{u}_g \right) \left(\boldsymbol{u}_\Gamma \cdot \boldsymbol{n}_\Gamma \right) dS = \int_{\Gamma} \left(-\left(p_l - p_g \right) \overline{\overline{\boldsymbol{I}}} + \left(\overline{\overline{\boldsymbol{\tau}}}_l - \overline{\overline{\boldsymbol{\tau}}}_g \right) + \overline{\overline{\boldsymbol{\tau}}}_\sigma \right) \boldsymbol{n} dS \tag{2.34}$$

By continuity in two phase flow, it was shown that $\boldsymbol{u}_\Gamma \cdot \boldsymbol{n}_\Gamma = 0$ in Eq. (2.19). Hence the left hand side is zero:

$$\int_{\Gamma} \left(-\left(p_l - p_g \right) \overline{\overline{\boldsymbol{I}}} + \left(\overline{\overline{\boldsymbol{\tau}}}_l - \overline{\overline{\boldsymbol{\tau}}}_g \right) + \overline{\overline{\boldsymbol{\tau}}}_\sigma \right) \boldsymbol{n} dS = 0 \tag{2.35}$$

From this relation, it directly follows that:

$$\boxed{\left(p_l - p_g \right) \overline{\overline{\boldsymbol{I}}} = \left(\overline{\overline{\boldsymbol{\tau}}}_l - \overline{\overline{\boldsymbol{\tau}}}_g \right) + \overline{\overline{\boldsymbol{\tau}}}_\sigma} \tag{2.36}$$

As shown by this relation, the effect of surface tension it to introduce a discontinuity in pressure and viscous effects in the interface.

Momentum conservation in separate phases

Following the same procedure of §2.2.2, the volumetric fraction is used to formulate momentum equations in strong form. Equation (2.28) can be applied to each phase for getting separate conservation equations of momentum. However, it must be taken into account that there can be exchange of momentum from one phase to another, something which was not taken into account in the mass equations because it is assumed that there is no mass exchange. This **momentum exchange** between both phases can be accounted for by adding a source term $\dot{\boldsymbol{s}}$. Then, the strong form of momentum conservation equations for each phase take the following form:

$$\frac{\partial \left(\alpha_g \rho_g \boldsymbol{u}_g \right)}{\partial t} + \nabla \left(\alpha_g \rho_g \boldsymbol{u}_g \boldsymbol{u}_g \right) = -\nabla \left(\alpha_g p_g \right) + \nabla \left(\alpha_g \overline{\overline{\boldsymbol{\tau}}}_g \right) + \alpha_g \boldsymbol{b}_g + \dot{\boldsymbol{s}}_g \tag{2.37a}$$

$$\frac{\partial \left(\alpha_l \rho_l \boldsymbol{u}_l \right)}{\partial t} + \nabla \left(\alpha_l \rho_l \boldsymbol{u}_l \boldsymbol{u}_l \right) = -\nabla \left(\alpha_l p_l \right) + \nabla \left(\alpha_l \overline{\overline{\boldsymbol{\tau}}}_l \right) + \alpha_l \boldsymbol{b}_l + \dot{\boldsymbol{s}}_l \tag{2.37b}$$

The integral balance can be obtained by integrating both expressions over a fixed control volume Ω and applying the Gauss theorem to the divergence term:

$$\frac{\partial}{\partial t} \int_\Omega \alpha_\mathrm{g} \rho_\mathrm{g} \boldsymbol{u}_\mathrm{g} dV + \int_{\partial\Omega} \alpha_\mathrm{g} \rho_\mathrm{g} \boldsymbol{u}_\mathrm{g} \left(\boldsymbol{u}_\mathrm{g} \cdot \boldsymbol{n} \right) dS = \int_{\partial\Omega} \alpha_\mathrm{g} \left(-p_\mathrm{g} \overline{\overline{\boldsymbol{I}}} + \overline{\overline{\boldsymbol{\tau}}}_\mathrm{g} \right) \boldsymbol{n} dS + \int_\Omega \alpha_\mathrm{g} \boldsymbol{b}_\mathrm{g} dV + \dot{\boldsymbol{S}}_\mathrm{g} \tag{2.38a}$$

$$\frac{\partial}{\partial t} \int_\Omega \alpha_\mathrm{l} \rho_\mathrm{l} \boldsymbol{u}_\mathrm{l} dV + \int_{\partial\Omega} \alpha_\mathrm{l} \rho_\mathrm{l} \boldsymbol{u}_\mathrm{l} \left(\boldsymbol{u}_\mathrm{l} \cdot \boldsymbol{n} \right) dS = \int_{\partial\Omega} \alpha_\mathrm{l} \left(-p_\mathrm{l} \overline{\overline{\boldsymbol{I}}} + \overline{\overline{\boldsymbol{\tau}}}_\mathrm{l} \right) \boldsymbol{n} dS + \int_\Omega \alpha_\mathrm{l} \boldsymbol{b}_\mathrm{l} dV + \dot{\boldsymbol{S}}_\mathrm{l} \tag{2.38b}$$

where $\dot{\boldsymbol{S}} = \int_{\partial\Omega} \dot{\boldsymbol{s}} dV$. The left hand side of these equations present two terms which are analogue to the ones in the continuity equations (2.22): a transient term accounting for the momentum variation within the control volume and a surface term accounting for the momentum fluxes entering or leaving the control volume through its boundaries. This term defines the **momentum flow rate**, or **momentum flux**, $\dot{M}$:

$$\boxed{\dot{\boldsymbol{M}} = \int_A \rho \boldsymbol{u} \left(\boldsymbol{u} \cdot \boldsymbol{n} \right) dS} \tag{2.39}$$

The right-hand side includes all the contributions from surface and body forces to the change of momentum of the system, plus the source term that will account for the momentum exchange between phases. The surface forces will be all group in the term $\boldsymbol{F}_s$, while the body forces will be denoted as $\boldsymbol{F}_b$. If the transient term of the left-hand side is called $\dot{\boldsymbol{J}}$ and the momentum fluxes are separated into inlet and outlet fluxes, then the momentum conservation for separated phases can be written as follows:

$$\boxed{\begin{aligned} \dot{\boldsymbol{J}}_{m_\mathrm{g}} &= \sum_{i_\mathrm{in}} \dot{\boldsymbol{M}}_{g_i} - \sum_{i_\mathrm{out}} \dot{\boldsymbol{M}}_{g_i} + \boldsymbol{F}_{s_\mathrm{g}} + \boldsymbol{F}_{b_\mathrm{g}} + \dot{\boldsymbol{S}}_\mathrm{g} \\ \dot{\boldsymbol{J}}_{m_\mathrm{l}} &= \sum_{j_\mathrm{in}} \dot{\boldsymbol{M}}_{l_j} - \sum_{j_\mathrm{out}} \dot{\boldsymbol{M}}_{l_j} + \boldsymbol{F}_{s_\mathrm{l}} + \boldsymbol{F}_{b_\mathrm{l}} + \dot{\boldsymbol{S}}_\mathrm{l} \end{aligned}} \tag{2.40a} \tag{2.40b}$$

2.3 Eulerian approaches for dense regime

Previously, the governing laws for fluid dynamics have been stated in their weak and strong forms. They have been extended to two-phase flows by introducing the volume fraction into the equations and by distinguishing between phases. It has been proved that surface tension introduces a discontinuity in the momentum equation, something the numerical method must deals with. This section presents several interface-capturing methods represented in Fig. 2.2 widely used to solve two-phase flow systems.

2.3.1 Diffuse interface methods

Diffuse interface is not formerly a method, but a family of them. The interface is not found at a precise spatial location, but is distributed along a transition region where both phases coexist. The liquid fraction of gas and liquid phases must add to 1: $\alpha_l + \alpha_g = 1$. Figure 2.3 shows a droplet solved with a diffuse interface method and a sharp interface (VOF) in the same grid, demonstrating clearly how the interface definition is straightforward in the latter b

A class of diffuse-interface methods arousing recent interest in immiscible, incompressible two-phase flows are the phase field methods. Originally, they make use of the Cahn-Hilliard equations (**?**). Their derivation is based on the minimisation of a free energy functional, which leads to a typical convection-diffusion equation with source terms. This equation presents the main disadvantage that it is written in a non-conservative form, and hence it is not suitable for its application in immiscible flows (**?**). This issue was later solved by **?**, who claimed that the following second order equation can be used with the same purpose and applied to immiscible flows:

$$\frac{\partial \psi}{\partial t} + \nabla \left(\mathbf{u} \psi \right) = \nabla \left[\gamma \left(\epsilon \nabla \psi - \psi \left(1 - \psi \right) \frac{\nabla \psi}{|\nabla \psi|} \right) \right] \tag{2.41}$$

where ϵ is a parameter defining the thickness of the interface, $\gamma = \max \left(\mathbf{u} \right)$ and ψ is a hyperbolic tangent function representing the distance from the interface, defined later in Eq. (2.48). This equation is transported to obtain the evolution of the interface with time. Then, the velocity fields are obtained from the traditional
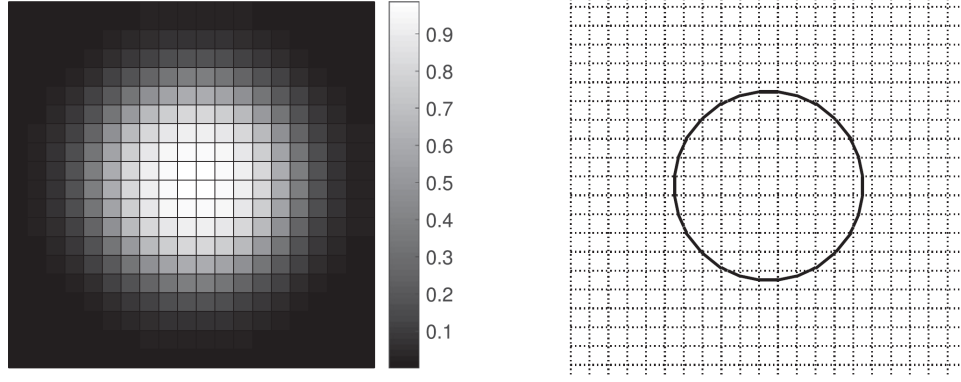
Figure 2.3: Comparison of a droplet solved in a 20x20 grid by a diffuse interface method (*left*) and a sharp-interface VOF method (*right*). Source: **?**

Navier-Stokes equations with a one-fluid formulation, Eq. (2.28). The density and viscosities are evaluated with the field function ψ:

$$\rho = \psi \rho_l - (1 - \psi) \, \rho_g \tag{2.42a}$$

$$\mu = \psi \mu_l - (1 - \psi) \, \mu_l \tag{2.42b}$$

Other available diffuse-interface methods have made use of the aforementioned Cahn-Hilliard and applied it to miscible flows (**?**) and to compressible two-phase systems (**?**). Furthermore, diffuse-interface methods find good applicability in particular thermodynamic regimes, such as multicomponent systems at supercritical conditions where surface tension is non-existent and a proper interface is not present (**??**).

2.3.2 Front-tracking method

The front-tracking method is, according to the classification of Figure 2.2, the only method presented in this chapter following an interface-tracking approach (the rest are comprised within the interface-capturing family). It was introduced for the first time by **?**. The interface is modeled as a moving front of lagrangian particles without mass which are explicitly tracked by connected marker points. Particles are convected with the flow field, and their movement is governed according to the kinematic equation:

$$\mathbf{u} = \frac{d\mathbf{x}}{dt} \tag{2.43}$$

where the velocity $\mathbf{u}$ is obtained by solving the flow field. As lagrangian particles are used, the interface is not solved in the same grid as the liquid and gas fields, see Fig. **??**. This makes this method more of a lagrangian nature than an eulerian one in the sense that the interface is resolved separately from the main grid. Yet, both phases are solved with an eulerian formalisms within the same grid, making this method eulerian since it aims mainly at solving separate-phase problems as indicated in Fig. 2.1 left. There are indeed interface-tracking methods dealing with the interface from an eulerian perspective, such as the Marker and Cell (MAC) method (**?**).

2.3.3 Volume of Fluid method

The Volume of Fluid method (VOF) is the first numerical methodologies developed to solve for liquid-gas interfaces in free surface flows, introduced originally by **?**. It is included among the methods using a **sharp-interface** approach, as opposed to diffuse interface which were succinctly discussed in the previous section. They have been extensively studied in literature , and have been applied for both structured (**??**) and unstructured (**??**) grids. VOF methods identify the liquid regions according to their liquid volume fraction α_l defined in Eq.(**??**). The volume fraction scalar is transported with an advection equation:

$$\frac{\partial \alpha_l}{\partial t} + \nabla \cdot (\alpha_l \boldsymbol{u}) = 0 \tag{2.44}$$
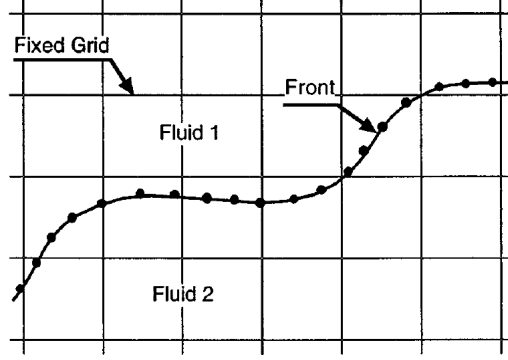
Figure 2.4: Illustration of the front-tracking method: both fluids are solved in the main grid while the interface is represented by a front of particles. Source: **?**

The material properties, density ρ and viscosity μ, are calculated from the liquid volume fraction:

$$\rho = \alpha_l \rho_l + (1 - \alpha_l) \rho_g \qquad (2.45a)$$

$$\mu = \alpha_l \rho_l + (1 - \alpha_l) \rho_g \qquad (2.45b)$$

The biggest advantage of VOF is the mass conservation, as it is ensured when solving 2.44. On the other side, its main challenge if the difficulty of reconstructing the interface from the transported α_l field, as illustrated in Figure 2.5. According to the approach used to reconstruct the interface, VOF methods can be classified as algebraic or geometric (**??**).
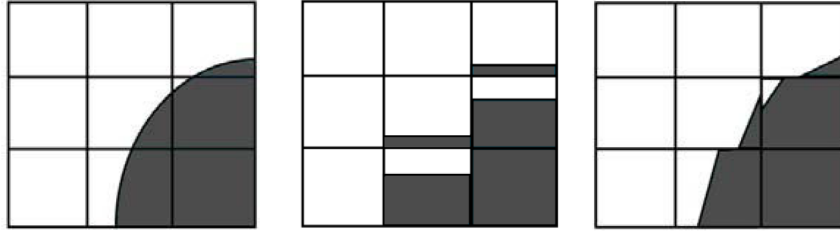
Figure 2.5: Application of VOF method, where dark is liquid and white is gas. *Left*: original α_l field. *Middle*: transported α_l field. *Right*: interface reconstruction, where a non-smooth interface can be appreciated. Source: **?**

2.3.4 Accurate Conservative Level Set method

A well-known class of interface-capturing approaches for two-phase flows are the level set methods. As their own name indicates, these methods identify the interface as a constant value of a scalar level set function. The interface is directly represented and transported using this function, hence its location is always known and no reconstruction needs to be done (as opposed to VOF methods).

Classical level set methods (**?**) distinguish between liquid and gaseous phases by introducing the smooth, signed-distance function to the interface $\phi(\mathbf{x}, t)$:

$$\phi(\mathbf{x}, t) = \pm |\mathbf{x}(t) - \mathbf{x}_\Gamma(t)| \qquad (2.46)$$

According to this definition, the interface is located at $\phi(\mathbf{x}, t) = 0$. Positive values of $\phi(\mathbf{x}, t)$ indicate liquid regions, while negative values denote gas. The interface is then transported with an advection equation:

$$\frac{\partial \phi}{\partial t} + \nabla \cdot (\phi \boldsymbol{u}) = 0 \qquad (2.47)$$

15

When applying the previous expression, the function ϕ will be distorted and its smoothness will be lost. To solvent this, the profile of ϕ is reshaped using a reinitialization equation (**?**) However, mass conservation is not ensured after the reinitialization process due to the nature of the distance function ϕ. In this sense, **?** tried to reduce the conservation errors by introducing the hyperbolic tangent function ψ:

$$\psi\left(\mathbf{x}, t\right) = \frac{1}{2}\left(\tanh\left(\frac{\phi(\mathbf{x}, t)}{2\varepsilon}\right) + 1\right) \tag{2.48}$$

where ε defines the interface thickness. The function ψ, which is a mapping from the classical signed-distance ϕ, is bounded between 0 and 1, while ϕ is unbounded. The interface Γ is located at the iso-value $\psi = 0.5$; gas phase is given by $\psi < 0.5$, and liquid for $\psi > 0.5$. Figure 2.6 shows a representative view of both distance functions.

As in the classical level-set method, the hyperbolic tangent profile is also transported via an advection equation:

$$\frac{\partial \psi}{\partial t} + \boldsymbol{\nabla} \cdot (\psi \mathbf{u}) = 0 \tag{2.49}$$

and then reinitialised through resolution of the following equation (**?**):

$$\frac{\partial \psi}{\partial \tau} = \boldsymbol{\nabla} \cdot (\ \underbrace{\varepsilon(\boldsymbol{\nabla}\psi \cdot \mathbf{n})\mathbf{n}}_{\text{Diffusion}} - \underbrace{\psi(1 - \psi)\mathbf{n}}_{\text{Resharpening}}\ ) \tag{2.50}$$

where τ is a pseudo-time and $\mathbf{n}$ is the normal vector to the interface, obtained from the signed-distance function ψ:

$$\mathbf{n} = \frac{\nabla\psi}{|\nabla\psi|} \tag{2.51}$$

As indicated in Eq. (2.50), the reinitialization process has two terms: diffusion and resharpening. Both of them are necessary to ensure the smoothness of ψ. With the introduction of ψ and the reinitialization equation, mass conservation errors are reduced: hence, this method is referred as conservative level set. Nevertheless, numerical errors might appear during reinitialisation since small oscillations in ψ might induce big variations in $\mathbf{n}$. To improve the accuracy, **?** proposed an extension to this conservative methodology in which the interface transport is solved with high order schemes and a fast-marching method is used to reconstruct the signed-distance function ϕ. This function is then used to compute the interface normals and, with it, the curvature κ:

$$\mathbf{n} = \frac{\nabla\phi}{|\nabla\phi|} \tag{2.52}$$

$$\kappa = -\nabla \cdot \mathbf{n} \tag{2.53}$$

? use a least squares reconstruction to compute κ. This extension to the conservative level set methodology is known as **Accurate Conservative Level Set** (ACLS) method. With these formulations, mass conservation is improved and numerical errors are reduced. ACLS is coupled to the Ghost-Fluid Method (GFM) (**?**) in order to deal explicitly with the pressure jump at the interface:

$$[p]_\Gamma = p_{l,\Gamma} - p_{g,\Gamma} = \sigma\kappa_\Gamma + 2\left[\mu\right]_\Gamma \mathbf{n}^T \cdot \nabla\mathbf{u} \cdot \mathbf{n} \tag{2.54}$$

where κ_Γ is the interface mean curvature and μ is the dynamic viscosity. Using this formulation, surface tension forces $\sigma\kappa_\Gamma$ are embedded in the pressure jump.

In this work, the more recent extension to the ACLS method by **ref:Janodet-2021-JCP** is used. This formulation makes use of the reinitialization equation introduced by **?**:

$$\frac{\partial \psi}{\partial \tau} = \boldsymbol{\nabla} \cdot \left(\frac{1}{4\cosh^2\left(\phi_{\text{map}}/2\varepsilon\right)}\left(|\boldsymbol{\nabla}\phi_{\text{map}} \cdot \mathbf{n}| - 1\right)\mathbf{n}\right) \tag{2.55}$$

where $\phi_{\text{map}} = \varepsilon\ln\left(\psi/(1 - \psi)\right)$ is an analytical signed-distance function mapped for $\psi \in]0; 1[$. This reinitialization equation ensures that the hyperbolic tangent profile ψ is reshaped after transport without introducing significant spurious displacement of the interface. The curvature is then calculated as follows:
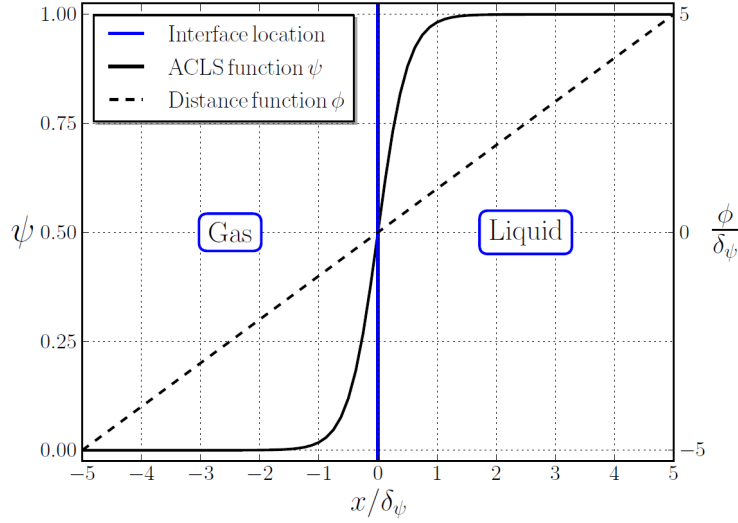
Figure 2.6: Representation of distance functions ϕ and ψ. The signed-distance function ϕ has been normalized by $\delta_\psi = 4\varepsilon$ for visualization. Source: **ref:Janodet-2021-JCP**.

$$\kappa = \frac{\mathrm{Tr}\left(\boldsymbol{\mathcal{H}}(\phi)\right) - \frac{\boldsymbol{\nabla}\phi^T}{|\boldsymbol{\nabla}\phi|} \cdot \boldsymbol{\mathcal{H}}\left(\phi\right) \cdot \frac{\boldsymbol{\nabla}\phi}{|\boldsymbol{\nabla}\phi|}}{|\boldsymbol{\nabla}\phi|} \tag{2.56}$$

where $\mathcal{H}\left(\phi\right)$ is the Hessian matrix of the distance function. To reduce numerical errors, a Geometric-Projection Marker Method (GPMM) is used reconstruct ϕ at the nodes in a narrow band around the interface (**?**). The GFM method is also used to deal with the interface pressure jump. Both phases are solved with a one-fluid formulation by solving Navier-Stokes and evaluating the physical properties at each spatial location with:

$$\rho(\mathbf{x},t) = \rho_g + (\rho_l - \rho_g)H(\psi(\mathbf{x},t) - 1/2) \tag{2.57a}$$
$$\mu(\mathbf{x},t) = \mu_g + (\mu_l - \mu_g)\psi(\mathbf{x},t) \tag{2.57b}$$

where H is the Heaviside function.

Coupling with dynamic mesh adaptation

To better resolve the atomization dynamics and save computational resources, the ACLS/GFM method is coupled to an Adaptive Mesh Refinement (AMR) strategy for increasing the mesh resolution at the liquid-gas interface at an affordable cost (**?**). In AMR, the target element size at the interface Δx_{min} and the number of cells with this size N_p are specified by the user. The spatial region containing elements with size Δx_{min} has a width $2N_p\Delta x_{\mathrm{min}}$, see Figure 2.7. The mesh is dynamically refined throughout the computation with an automatic distance-based triggering ensuring that the interface always remains within this region. In its vicinity, the cell size increases linearly with controlled slope until the baseline cell size Δx_{init}. AMR will be used in all the resolved atomization simulations presented in this thesis. Hence, the full methodology used to performed this simulations will be referred from now on as ACLS/AMR.
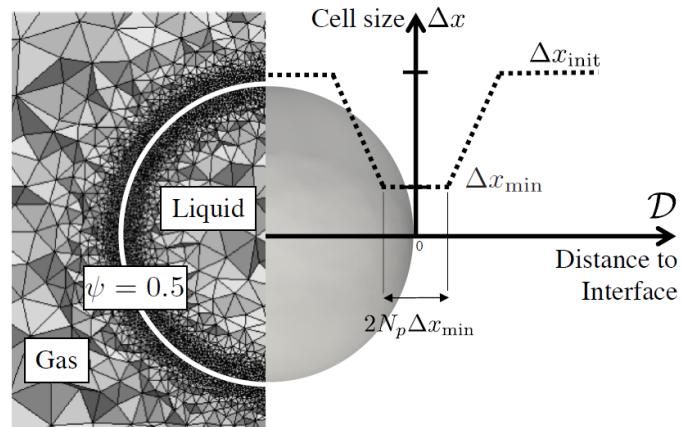
Figure 2.7: Illustration of dynamic mesh adaptation with Adaptive Mesh Refinement. Source: (**?**).

Chapter 3

Numerical methods to simulate dispersed phase

3.1 Introduction

The previous chapter presented numerical methodologies applicable to separate two-phase flows. These are useful for solving problems where the dynamics of atomization need to be accurately resolved. Nonetheless, those methods cannot be applied in the dispersed phase regime, where atomization is complete (or almost complete) and a spray composed of individual droplets is formed. Such problems, often found when studying reactive processes where fuel is injected into a combustion chamber, need a different representation of the liquid phase so that 1) the spray can be transported with acceptable computational costs and 2) can include more complex physics relevant to reactive problems, such as evaporation and combustion.

The spray generated in the dispersed phase regime is mainly distinguished from liquid in the separate regime by the following features (represented in Figure 1.5):

- The characteristic length scales of the particles. In dispersed phase flows, these ones are low and usually smaller than the resolution of the main grid.

- The value of the liquid volume fraction α_l. In dispersed phase flows, $\alpha_l < 1$. According its value, one can distinguish between dense regime (moderate values of α_l, particles are close to each other) and dilute regime (lower values of α_l, usually below 10^{-3}, particles are far from each other).

The numerical formalisms to resolved dispersed phase flows will hence depend on these two characteristics. It is also important to consider the interaction with the gaseous phase, since this one will depend by the resolution of the main grid. The interaction between the liquid and gaseous phases in dispersed phase flows can be quantified by means of the Stokes number St, defined as the ratio between the characteristic time-scale of a liquid particle τ_p and a characteristic time of the gaseous phase τ_g:

$$St = \frac{\tau_p}{\tau_g} \tag{3.1}$$

A classification of numerical methods to simulate dispersed phase flows based on the volume fraction and the Stokes number has been done by **ref:2009-Balachandar**, shown in Figure 3.1. As it can be seen, the Stokes number will depend on the numerical methodology used to resolve the gaseous phase: in DNS, the smallest scales of turbulence with characteristic size η will be resolved and will have a characteristic time τ_k, while in LES the smallest scales resolved ξ will be larger and their time-scales will be different (τ_ξ). Regarding the volume fraction, coupling strategies between liquid particles and gas can be used depending on its value: in the dilute regime particles are far from each other and the interactions among them can be neglected (one and two-way coupling), while in the dense regime the interaction between particles must be taken into account (four-way coupling). The difference between one and two-way coupling depends on if the influence of the liquid phase onto the gas is considered with source terms (two-way coupling) or if it is neglected, so that the gaseous phase will not be perturbed by the particles (one-way coupling).
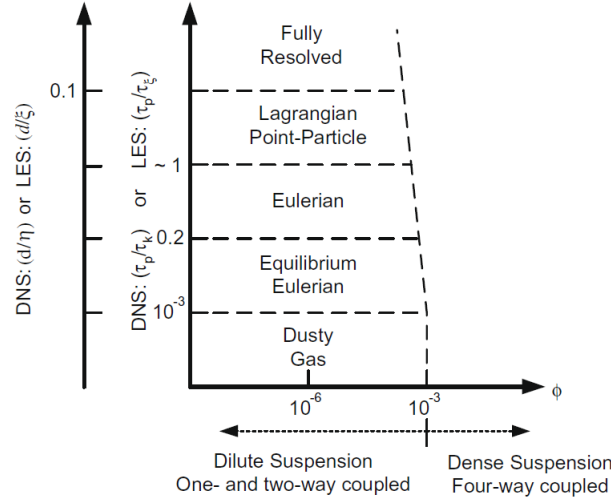
Figure 3.1: Several numerical approaches to solve dispersed phase flows. Classification is done with respect to the liquid volume fraction (here defined as ϕ) and to the Stokes number or, equivalently, to the ratio of largest to smallest length scales, which depend on the numerical resolution. Source: **ref:2009-Balachandar**

3.1.1   Existing approaches to model dispersed phase flows

Several approaches exist to study disperse phase.

Comment statistical approaches (2000 SUbramanian, 2013 Vie, Vie 2013). Mention that they are out of the scope of this thesis, so we are gonna focus on EE and EL.

In this chapter,

3.2   Eulerian formalisms for dispersed phase

One common numerical method to solve

An Eulerian description of the fluid flow (EE) takes a control volume and averages the properties of the fluid flow within it. Both the carrier and dispersed phase are resolved in the same grid, which can save computational time. For characterizing the dispersed phase, averaged properties and statistical tools are used to solve the Navier-Stokes equations. It presents, however, the following disadvantages (**?**):

1. A non-robust system of equations is produced.

2. Interactions of the particles with the walls and among themselves are very difficult (if not impossible) to model.

The carrier phase is solved from the Navier-Stokes equations (**??**) applied to gas, neglecting the conservation of species as there are no chemical reactions. In order to develop the equations for the disperse, the following assumptions need to be made (**?**):

1. The atomization process is complete: no further breakup occurs, and the particles are perfectly spherical droplets.

2. The density ratio between gas and liquid allows to assume that the only force exerted by the carrier phase on the droplets is drag.

3. The temperature, and therefore the sensible enthalpy, is assumed to be homogeneous inside each droplet.

4. A dilute spray assumption is made ($\alpha_l < 0.01$), so the liquid volume fraction is negligible before the gaseous one: $\alpha_g = 1 - \alpha_l \approx 1$. This leads to the next two hypotheses.

5. The interactions between droplets are negligible.

6. The liquid phase has little influence over the carrier phase, which allows the use of a probability density function conditioned by one realization.

7. The spray is mono-disperse and mono-kinetic: at one point in time and space, the droplets all have the same diameter and velocity.

8. Similarly, at one point in time and space, the droplets have the same temperature.

For the disperse phase, the corresponding equations are:

$$\frac{\partial \breve{n}_l}{\partial t} + \frac{\partial \breve{n}_l \breve{u}_{l,i}}{\partial x_i} = 0 \tag{3.2a}$$

$$\frac{\partial \rho_l \breve{\alpha}_l}{\partial t} + \frac{\partial \rho_l \breve{\alpha}_l \breve{u}_{l,i}}{\partial x_i} = -\Gamma \tag{3.2b}$$

$$\frac{\partial \rho_l \breve{\alpha}_l \breve{u}_{l,j}}{\partial t} + \frac{\partial \rho_l \breve{\alpha}_l \breve{u}_{l,i} \breve{u}_{l,j}}{\partial x_i} = \mathcal{T}\left(u''_{p,j}\right) - \Gamma \breve{u}_{l,j} + F_{d,j} \tag{3.2c}$$

$$\frac{\partial \rho_l \breve{\alpha}_l \delta \breve{\theta}_l}{\partial t} + \frac{\partial \rho_l \breve{\alpha}_l \breve{u}_{l,i} \delta \breve{\theta}_l}{\partial x_i} = \mathcal{T}\left(\frac{1}{2} u''_{p,j} u''_{p,j}\right) + \mathcal{U}_\theta - \Gamma \delta \breve{\theta}_l + W_\theta \tag{3.2d}$$

$$\frac{\partial \rho_l \breve{\alpha}_l \breve{h}_{s,l}}{\partial t} + \frac{\partial \rho_l \breve{\alpha}_l \breve{u}_{l,i} \breve{h}_{s,l}}{\partial x_i} = \Lambda_l + \Phi_l \tag{3.2e}$$

Details on the equations and on their terms is not given here, as the EE method will not be used in this project. A more rigorous explanation of this model can be found in **?** and in **?**.

3.3 Lagrangian point particle representation

The Lagrangian description (EL) does not use an averaging process in the grid for the fluid phase, but tracks each fluid particle individually. Every droplet is represented by its own equations which are not solved in the main grid (i.e. the Eulerian grid used to represent the carrier phase). This can make convergence difficult and hinders the introduction of parallelism techniques. However, the resulting system of equations is robust, the time per iteration is usually lower than for the EE description, and the drop-drop and drop-wall interactions are easier to model.

When considering droplets immersed in a gas, it is necessary to take into account mechanics of particle motion. A useful definition to study the relative influence between the droplet and the gas is the **Stokes number**, which is defined as the ratio between the characteristic time of the particle τ_p and the frequency of the flow fluctuations f_{turb} around an obstacle (**?**):

$$St = \tau_p f_{turb} = \frac{\tau_p \widetilde{\boldsymbol{u}}_g}{d_p} \tag{3.3}$$

where $\widetilde{\boldsymbol{u}}_g$ is the gas velocity at the position of the particle p assuming that the flow field is locally undisturbed by the presence of that particle. The Stokes number indicates how the droplet responds to fluctuations of the gas flow. If $St << 1$, the droplet will follow perfectly the fluctuations of the gas flow. On the contrary, if $St >> 1$ the droplets will rather neglect the flow trajectories and follow a ballistic trajectory. τ_p is obtained from the following expression (**CHECK THIS OUT**):

$$\tau_p = \frac{d_p^2 \rho_p}{18\mu_g} = \frac{4}{3}\frac{\rho_p}{\rho_g}\frac{d_p}{C_D |\boldsymbol{v}_r|} = \frac{4}{3}\frac{\rho_p d_{p^2}}{\mu_g Re C_D} \tag{3.4}$$

For the description in the Lagrangian framework, each particle will be modelled according to the **Discrete Particle Simulations** (DPS) approach. DPS assumes each particle to be completely spherical and robust. With these assumptions, the **dynamic equations** for a particle p in the spatial direction i are:

$$\frac{d\boldsymbol{x}_p}{dt} = \boldsymbol{u}_p \tag{3.5a}$$

$$\frac{d\boldsymbol{u}_p}{dt} = \underbrace{-\frac{3}{4}\frac{\rho_g}{\rho_p}\frac{C_D}{d_p}|\boldsymbol{v}_r|\boldsymbol{v}_r}_{\text{Drag term}} + \underbrace{\left(1 - \frac{\rho_g}{\rho_p}\right)\boldsymbol{g}}_{\text{Gravity term}} \tag{3.5b}$$

where ρ_g and ρ_p are the gas and liquid particle densities respectively, C_D is a drag coefficient, d_p is the particle diameter, $\boldsymbol{v}_r$ is the relative velocity of the particle with respect to the airflow and g is the gravity term. Equation (3.5b) is the momentum equation of the droplet and contains the contributions of the two forces considered: the drag force and the gravitational forces. The relative velocity is given by $\boldsymbol{v}_r = \boldsymbol{u}_p - \widetilde{\boldsymbol{u}}_g$

The drag coefficient C_D is given by the following expression:

$$C_D = \begin{cases} \dfrac{24}{Re}\left(1 + 0.15 Re^{0.687}\right) & \text{if } Re < 1000 \\ 0.44 & \text{if } Re \geq 1000 \end{cases} \tag{3.6}$$

where $Re = \rho_g|\boldsymbol{v_r}|d_p/\mu_g$. This expression was obtained experimentally by **?** with the assumptions that the particles are perfectly spherical and rigid.

Besides the dynamic equations, it is also necessary to account for the **phase transition** of the liquid dispersed phase into gaseous phase.

$$\frac{dm_p}{dt} = \dot{m}_p = \Gamma \tag{3.7a}$$

$$\frac{dh_p}{dt} = \Phi_p \tag{3.7b}$$

Equation (3.7a) accounts for the **evaporation** process. If the uniform temperature model is used, then (3.7) is equal to (**??**). Equation (3.7b) accounts for the energy transfer. By considering the effects of the **conduction** and the **evaporation** processes in terms of energetic balance, Φ_p can be extended as follows:

$$\Phi_p = m_p C_{P_g}\frac{dT_p}{dt} = \underbrace{h_p \pi d_p^2\left(T_g - T_p\right)}_{\text{Conduction term}} - \underbrace{\dot{m}_p \Delta h_v}_{\text{Evaporation term}} \tag{3.8}$$

where C_{P_g} is the gas specific heat capacity at constant pressure, T_p is the particle temperature, T_g is the gas temperature, h_p is the film coefficient of the gas at the particle surface and Δh_v is the latent heat of vaporization of the particle.

By considering Equations (3.5) and (3.7) with all the simplifications stated, the final set of equations for the Lagrangian dispersed phase approach is:

$$\frac{dx_{p,i}}{dt} = u_{p,i} \tag{3.9a}$$

$$\frac{du_{p,i}}{dt} = -\frac{u_{p,i} - \widetilde{u}_{g,i}}{\tau_p} + \left(1 - \frac{\rho_g}{\rho_p}\right)g_i \tag{3.9b}$$

$$\frac{dm_p}{dt} = \Gamma \tag{3.9c}$$

$$m_p C_{P_g}\frac{dT_p}{dt} = h_p \pi d_p^2\left(T_g - T_p\right) - \dot{m}_p \Delta h_v \tag{3.9d}$$

3.4 Lagrangian injection models for multipoint injection

A classification of models for liquid injection in dispersed phase computations is proposed in Figure 3.2.

3.4.1 Airblast spray

Basically Chaussonnet.
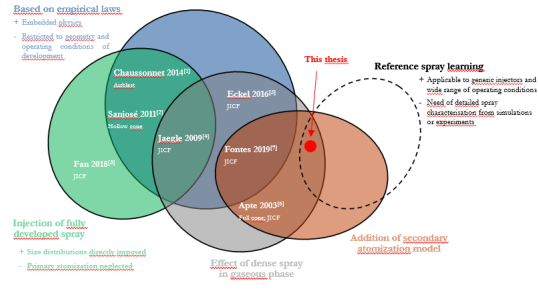
Figure 3.2: Classification of lagrangian injection models

3.4.2 Hollow cone spray

Basically FIMUR.

3.4.3 Liquid jet in crossflow

Aqui viene el arsenal.

Part II

Building lagrangian injectors from resolved atomization simulations

Chapter 4

Models for lagrangian injection

Describe here the flowchart of our models and their ingredients. If other models are developed, add them here too.

- Flowchart

- Spray definition: with f function ? Or with lagrangian formalisms ?

- Spray sampling (reference to chapter JICF resolved simulations)

- Spray convergence (MSE error definition [mention to Cramer-von Mises], quadtrees local refinement ...)

- Injectors creation (spatial refinement, quadtrees local refinement,)

- Secondary atomization models.

- Actuator line method for dense core modelling

4.1 Introduction

4.2 Description of sprays

4.3 Models flowchart

The flowchart of the models is shown in Figure 4.1. The main workflow of information to build lagrangian injectors is shown in the central part of the figure, where each block is explained in a different chapter of this manuscript:

1. Resolved atomization simulations are performed to build a database (Chapter **??**).

2. This database is used and processed by the models to learn the spray state and build lagrangian injectors (Chapter 4).

3. Lagrangian simulations are initialized with the injectors developed with this methodology (Ch. 6)

    Additionally, there are more submodels to take into account:

- The bottom row represents the processes comprising the learning part of the lagrangian injectors: spray sampling (§4.4.1), spray convergence (§4.4.2) and spatial discretization of the injectors (§4.4.3).

- The top boxes represent the submodels that add more detailed physics into the methodology. Currently there are two:

– **Dense core learning** in order to take into account the perturbation effect of the liquid dense structures (i.e. the liquid dense core in the JICF) in the gaseous phase during lagrangian simulations (§4.5). The information to characterize the dense core is taken from the resolved simulations and later imposed into lagrangian ones.

– **Secondary atomization models** to consider further possible breakup of spherical droplets during lagrangian simulations § 4.5).
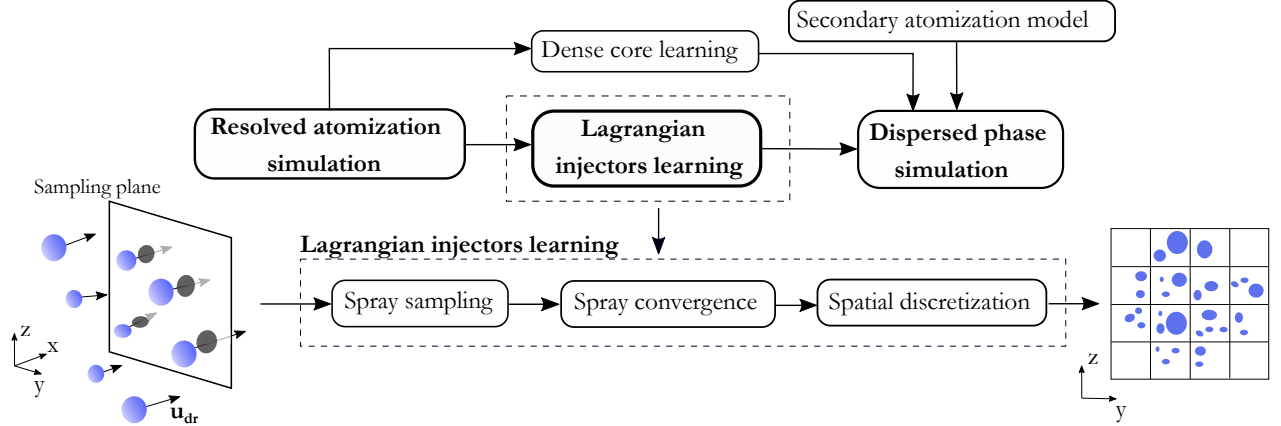
Figure 4.1: Flowchart for proposed models of lagrangian injection.

4.4 Lagrangian injectors learning

4.4.1 Spray sampling

Identification of liquid structures in resolved simulations

The first step in the learning process is to obtain the spray from resolved atomization simulations. For this purpose, droplets must be identified in space. According to the ACLS methodology (§2.3.4), liquid regions are identified by values of the level set $\psi > 0.5$, and the interface Γ is located at $\psi = 0.5$. It is possible then to identify and tag individual liquid structures as independent closed regions of Γ, whose domain is denoted as Ω_l. Each structure can then be characterized by its volume V_{dr}, its center of mass location $\mathbf{x}_{\mathrm{dr}}$ and velocity $\mathbf{u}_{\mathrm{dr}}$, and maximum and minimum distances from the interface to the center of mass $R_{\max}$ and $R_{\min}$, as depicted in Figure 4.2. The formulas used for calculating these parameters are shown in Table 4.1.

Table 4.1: Parameters sampled from resolved atomization simulation

Parameter	Definition	Description
V_{dr}	$\displaystyle\int_{\Omega_l} d\mathbf{x}$	Volume enclosed by interface
$\mathbf{x}_{\mathrm{dr}}$	$\displaystyle\frac{1}{V}\int_{\Omega_l} \boldsymbol{x}\, d\mathbf{x}$	Location of center of mass
$\mathbf{u}_{\mathrm{dr}}$	$\displaystyle\frac{1}{V}\int_{\Omega_l} \mathbf{u}\left(\boldsymbol{x}\right) d\mathbf{x}$	Velocity of center of mass
$r_{\max}$	$\max\left(\mathbf{x} - \mathbf{x}_{\mathrm{dr}}\right) \forall \mathbf{x} \in \Omega_l$	Maximum distance to center of mass
$r_{\min}$	$\min\left(\mathbf{x} - \mathbf{x}_{\mathrm{dr}}\right) \forall \mathbf{x} \in \Omega_l$	Minimum distance to center of mass

In order to get statistics for spray characterization, it is useful to define a characteristic size of each liquid structure. For this purpose, an equivalent radius R_{dr} is calculated from the liquid volume V:

Figure 4.2: Parameters characterizing liquid structures sampled in resolved atomization simulations.

$$r_{\mathrm{dr}} = \sqrt[3]{\frac{3V_{\mathrm{dr}}}{4\pi}} \tag{4.1}$$

which is the radius of a sphere containing the same volume as the structure. The equivalent diameter is then $d_{\mathrm{dr}} = 2r_{\mathrm{dr}}$ In cases where sampled structures are spherical droplets, R_{dr} is the true radius and, therefore, a representative measure of the droplets' size. On the othe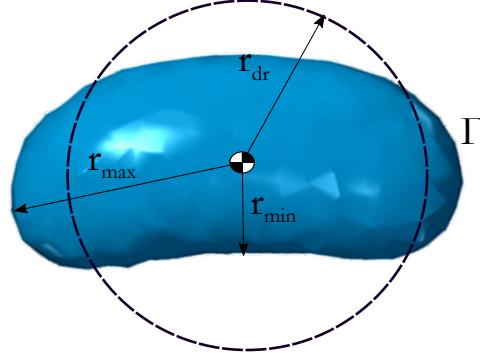r hand, if liquid structures are not fully spherical (which is specially true after primary atomization), the equivalent radius does not provide full information on their topology. To determine the deviation of the identified liquid structure from a sphere, the radii $r_{\max}$ and $r_{\min}$ can be used to calculate the deformation parameters α and β (**?**):

$$\alpha = \frac{r_{\max}}{r_{\mathrm{dr}}} \quad ; \quad \beta = \frac{r_{\min}}{r_{\mathrm{dr}}} \tag{4.2}$$

By definition, $\alpha \geq 1$ and $\beta \leq 1$. A perfect sphere would present $\alpha = \beta = 1$.

In this work, no distinction between droplets and ligaments has been done to construct the injectors after the learning procedure. Hence, hereafter all liquid structures will be referred as droplets, and the term droplet sampling will be used. Inclusion of distinction between ligaments and droplets (i.e. between non-spherical and spherical structures) could be further taken into account with parameters α and β to, for example, modifying drag coefficients in lagrangian simulations at the first steps after injection (**?**).

Sampling procedure

Droplets are sampled according to their center of mass location. Note that, despite the ACLS methodology being eulerian, liquid structures produced by resolved simulations are being tracked as lagrangian particles (lagrangian tracking). Two sampling methods based on experimental techniques can be used (**?**), their main difference being the topology of the employed probes (see Figure 4.7):

- A control volume (unit volume in Figure 4.7) can be defined where particles contained inside are sampled at a particular time instant. This method produces a **volume distribution**.

- A surface area (unit area in Figure 4.7) or plane where droplets crossing it during a given time are sampled. A **flux density distribution** is obtained in this case.

In this work, droplets crossing surface areas are sampled, hence obtaining flux density distributions. The defined surface areas employed will be hereafter referred as **sampling planes**. Spray is sampled from resolved atomizations with a sampling rate ensuring that all droplets crossing the plane are collected. Droplets are
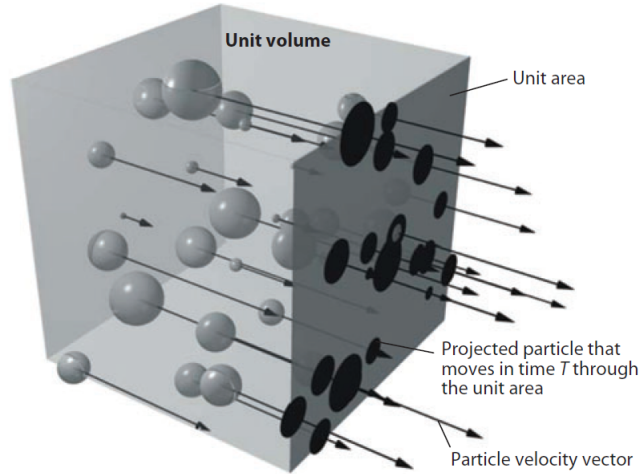
Figure 4.3: Droplet sampling prodecure. Source: **?**

then accumulated with time, and then statistics are calculated. Choosing a right sampling rate will ensure that at the end of the accumulation process, the mass flow rate in average is the actual rate passing through the sampling plane in the resolved simulations. If the sampling rate is too low, some droplets might be missed and the flow rate captured will not be the right one (*aliasing* phenomenon on the spray sampling procedure). Another technique to measure flow rates directly in resolved atomization simulations, called interior boundaries, has been developed in this thesis. It is later explained, and compared to the rates obtained from the lagrangian tracking procedure, in §5.4.3.3.

4.4.2 Spray convergence

Simulations using the ACLS/AMR methodology can resolve the atomization process and provide deep insight on the driving physical phenomena. Nevertheless, their main limitation is their cost (see §5.4.6), which increases when more liquid is present in the domain and more droplets are formed. Consequently, the accumulation time of droplets will be finite and, logically, restricted to the physical time being simulated. This can pose a problem when characterizing the spray, since statistics might be converged if the number of sampled droplets is not sufficient.

With this issue in mind , a methodology to evaluate spray convergence is proposed. The objective is to provide a quantitative measure to assess whether enough droplets have been sampled to obtain reliable statistics (**?**). If the spray is converged, then it can be spatially discretized to get local statistics that will conform the injectors (§4.4.3). This convergence criterion is also used to propose another discretization strategy in which refinement is performed following a quadtrees structure (convergence-driven discretization, see §4.4.4).

At each time step t_i of the accumulation process, the spray will be formed by a number of droplets $N_{\mathrm{dr},i}$. This number will increase as more particles are accumulated with time, since all droplets sampled previously are also accounted for (hence the name accumulation). One can see this methodology as obtaining a time-averaged spray, since dependence with time is neglected. Statistics can be calculated on the accumulated spray at each time t_i, such as the droplet histogram. Figure 4.4 left shows an illustrated view of the size histogram evolution at several accumulation instants. The histogram indicates thes probability $f(d_{\mathrm{dr}})$ of finding a droplet of size d_{dr} within a class n: $d_{\mathrm{dr}} \in [d_{\mathrm{dr},n} - \Delta d_{\mathrm{dr}}, d_{\mathrm{dr},n} + \Delta d_{\mathrm{dr}}]$. Its shape will change with the accumulation time until a time when it will not change once more droplets are sampled. At this point, the spray will be considered to be converged.

The main issue now is to determine quantitatively when the spray is converged. For this purpose, the histograms are compared in pairs at subsequent time instants, t_i and t_{i-1}, as shown in Figure 4.4 right. The same number and width of droplets classes are used in both histograms. The difference between both histograms is then measured by means of a Mean Squared Error (MSE) function defined as:

$$MSE^{t_i} = \frac{1}{N} \sum_{n=1}^{N} \left(f_n^{t_{i-1}} - f_n^{t_i} \right)^2 \tag{4.3}$$

where N is the total number of classes in the histogram. This criterion is similar to the Carmen-von Mises measure to compare two statistical distributions (**?**). The MSE can then be calculated at each accumulation time instant and then be normalized by the maximum value obtained, yielding a Normalized Mean Squared Error (NMSE) (**?**):

$$NMSE^{t_i} = \frac{MSE^{t_i}}{\max_{t_i}(MSE)} \tag{4.4}$$

The evolution of NMSE can be displayed with time as shown in Figure 4.5. The NMSE decreases with accumulation time until reaching a plateau, where the ?NMSE does not move significantly. Convergence is achieved at this plateau, which is defined for values of the NMSE below a threshold ε_{th}.

$$NMSE < \varepsilon_{\text{th}} \tag{4.5}$$

where ε_{th} is set to 0.01 (i.e. 1%).
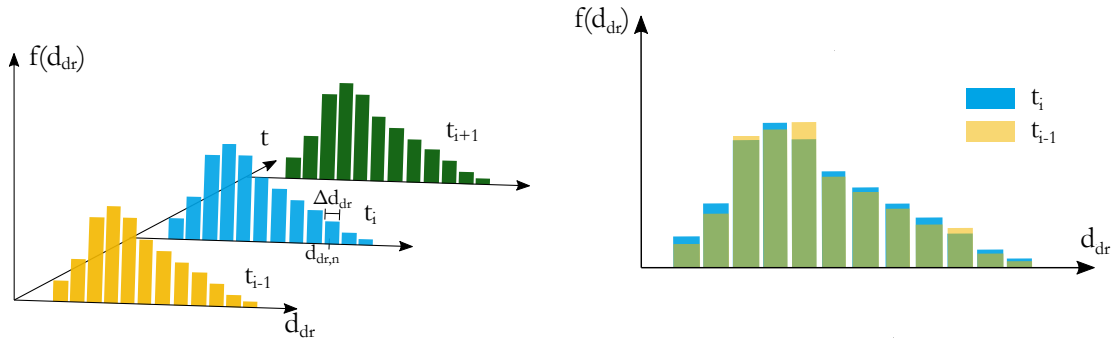
Figure 4.4: *Left*: Size histogram evolution with accumulation time of droplets. *Right*: comparison of two droplet size histograms from two consecutive time instants.
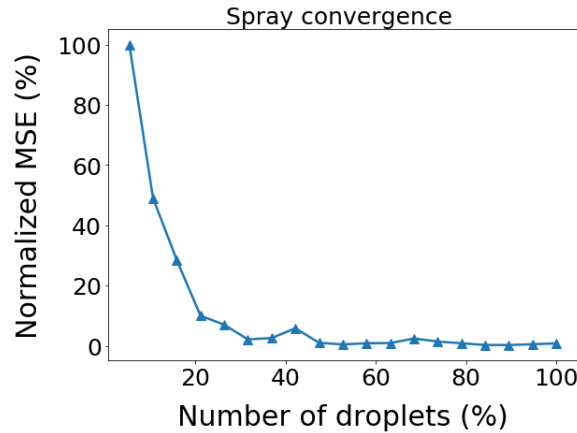
Figure 4.5: Evolution or Normalized Mean Squared Error (NMSE) with respect to the spray accumulation time. **IMPROVE THIS**

It is worth noting that the convergence criterion based on NMSE introduced in this section depends solely on the equivalent droplets size d_{dr}. Future work would include to extend this criterion to other magnitudes fundamental for a proper spray representation, such as velocities and flow rates.

Furthermore, a time-independent spray has been considered in all the previous process by accumulating droplets and calculating statistics which do not depend on the time in which they were sampled. A perspective

in this respect would be to obtain a transient spray in order to create unsteady numerical injectors. This could be useful in systems where thermoacoustic instabilities appear and there are fluctuations in the injected flow rates, such as aeronautical gas turbines (**?**).

4.4.3 Spatial discretization of sprays
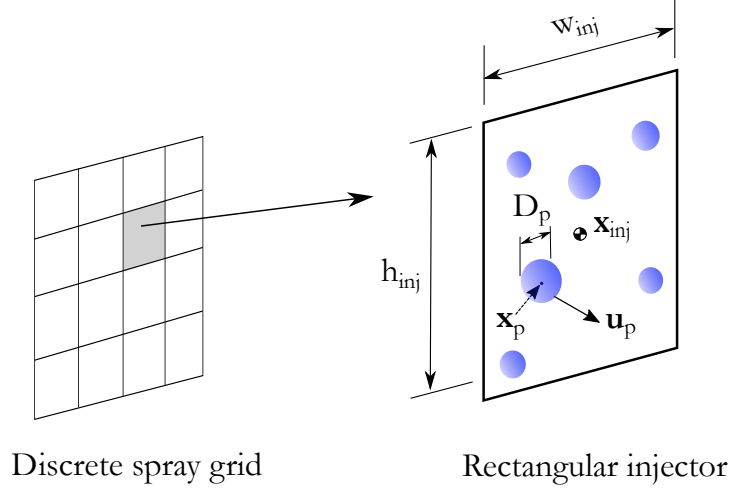
Figure 4.6: Injection parametrization

4.4.4 Convergence-driven discretization

4.4.4.1 Theory and concepts

4.4.4.2 Numerical implementation

The numerical implementation of the process works as follows:

1. From global spray, create a 3x3 grid (**parent grid**).

2. From global spray, create a 6x6 grid (**children grid**).

3. Map children elements to parent elements to check local convergence:

   (a) If all children elements belonging to parent element are converged, **refine**: keep statistics from 6X6 grid.

   (b) If not all children elements are converged, then **unrefine**: store parent elements characteristics into grid (mean and RMS velocities, SMD, volume flux), and divide flux by 4.

4.4.5 Injectors definition

Statistics are obtained

Time-averaged and RMS parameters are of a quantity f are defined respectively as follows:

$$\overline{f} = \frac{1}{T} \sum f\left(t_i\right) \delta t_i \tag{4.6}$$

$$f_{\text{RMS}} = \sqrt{\overline{f^2} - \overline{f}^2} \tag{4.7}$$

Injection location

Injection velocity

Velocity at injection can be specified as follows:

$$\boldsymbol{u}_{\mathrm{p}} = \overline{\boldsymbol{u}} \tag{4.8}$$

$$\boldsymbol{u}_{\mathrm{p}} = \overline{\boldsymbol{u}} + \boldsymbol{r}^T \boldsymbol{u}_{RMS} \tag{4.9}$$

$$\overline{\boldsymbol{u}} = \begin{pmatrix} \overline{u} & \overline{v} & \overline{w} \end{pmatrix}^T \tag{4.10}$$

$$\boldsymbol{u}_{Inj} = \begin{pmatrix} \overline{u} & \alpha\overline{v} & \alpha\overline{w} \end{pmatrix}^T \tag{4.11}$$

$$\boldsymbol{u}_{RMS} = \begin{pmatrix} u_{RMS} & v_{RMS} & w_{RMS} \end{pmatrix}^T \tag{4.12}$$

$$\boldsymbol{u}_{\mathrm{p}} = \begin{pmatrix} \overline{u} & 0 & 0 \end{pmatrix}^T \tag{4.13}$$

$$\boldsymbol{u}_{\mathrm{p}} = \boldsymbol{u}_{Gas} \tag{4.14}$$

where $\boldsymbol{r}$ is a vector of random numbers $\in [-\sqrt{3}, \sqrt{3}]$, and $\overline{\boldsymbol{u}}$ and $\boldsymbol{u}_{RMS}$ are respectively the mean and RMS velocities of the sampled droplets at the injection element.

$$\boldsymbol{r} \sim \mathcal{N}\left(\mu = 0, \sigma = 1\right) \tag{4.15}$$

Volume-weighting the velocity

As it is later shown in §**?**, the droplets mean velocities can be weighted by their mean profiles:

$$\langle \mathbf{u} \rangle_V = \frac{\sum i = 1^{N_{\mathrm{dr}}} \mathbf{u}_i V_i}{\sum i = 1^{N_{\mathrm{dr}}} V_i} \tag{4.16}$$

In the same fashion, the RMS can also be "volume-weighted" by applying the former expression:

$$\mathbf{u}_{RMS,V} = \sqrt{\langle \mathbf{u}^2 \rangle_V - \langle \mathbf{u} \rangle_V^2} \tag{4.17}$$

Injector topology

4.5 Dense core blockage effect modeling

One key point of the resolved atomization simulations is that they can account for the liquid-gaseous interaction without the need to be modelled or accounted for with source terms in the governing equations. This allows that the perturbation effects from the gas to the liquid, which influence spray dispersion, can be properly captured. In the jet in crossflow this influence is paramount, since the liquid coherent structures impose a blockage effect to the gaseous phase that creates vortical structures downstream the liquid injection nozzle (see Figure **??** and §5.4.4).

These perturbations effects are not taken into account *a priori* in dispersed phase simulations, since the coherent structures are not present. Some approaches have succeeded in emulating this interaction between phases by injecting lagrangian big droplets according to the the blob method (**?**) and adding a two-way coupling between liquid and gaseous phases (**??**). Other studies have solved and kept the liquid coherent structures with VOF to capture the interaction, and then performed lagrangian injection and spray transport (**??**).

In this work, the blockage effect is modeled in dispersed phase computations by means of the Actuator Line Method (ALM). This method has been, to the author's knowledge up to date, in wind turbine simulations for representing the effect of the tower and blades in the gaseous field, which creates strong turbulence. Firstly, a review on the theory and some previous works in ALM is done. Secondly, the way ...

4.5.1 Actuator Line Method

As shown in Fig. (**Ref. to figure in introduction**), the dense core has a perturbation effect towards the gas phase. This is accounted for with the Actuator Line Method (ALM): **Sorensen 2002**, **Benard 2018**, **Houtin-Mongrolle 2020**.

4.5.2 Dense core representation as an actuator

4.5.3 Forces determination

4.6 Secondary atomization modeling

In disperse phase simulations, spray is modeled by a set of spherical and rigid particles whose dynamics are governed by the point-particle equations described in §3.3. Due to these assumptions, particles will not break by their interaction with the gaseous phase as in the resolved atomization simulations. Nevertheless, further breakup can be taken into account by means of secondary atomization models. The most important parameter governing secondary atomization is the Weber number based on the relative velocities between liquid and gas u_{rel}:

$$We = \frac{\rho_g u_{\text{rel}}^2 r}{\sigma} \tag{4.18}$$

Different mechanisms produce secondary atomization depending on the value of We, see Fig. **ref:fig??**. Existing models for secondary atomization have been developed for each particular mode of breakup, such as the WAVE model for high Weber numbers (**?**) or the Taylor Analogy Breakup (TAB) model for low ones (**?**). The former model predicts breakup by following a linear stability analysis considering Kelvin-Helmholtz waves as the governing breakup mechanisms, while the latter makes an analogy between a droplet and a second-order mechanical system. Nevertheless, up to date there is not a model which accounts for all different breakup mechanisms and that can capture all the physical complexity of secondary atomization.

In this work, three atomization models have been implemented and tested: the TAB model, the Enhanced TAB model (**?**), and the stochastic model of **?**. They are described in the following sections.

4.6.1 Taylor Analogy Breakup
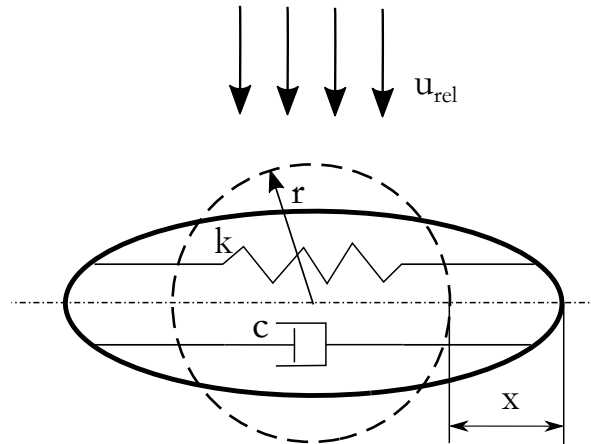
Figure 4.7: Taylor analogy breakup between a droplet and a mechanical system with spring and damper. The undeformed droplet is represented by the dashed line, while the thick solid line depicts the droplet after deformation. x is the displacement from the deformed to the undeformed states.

The Taylor Analogy Breakup (TAB) model is one the first secondary atomization models. Developed by **?**, it makes an analogy between a droplet and a mechanical system as shown in Fig. 4.7. Breakup occurrence

is estimated by solving the ordinary differential equation (ODE) representing the oscillating dynamics of the mechanical system depicted:

$$m\ddot{x} = F - kx - c\dot{x} \tag{4.19}$$

where x is the displacement from the droplet's equator due to deformation, m is the mass, F is the external force, k is the spring constant and c is the damping coefficient. The Taylor analogy makes a comparison between this mechanical system and the droplet, producing the following relation between constants:

$$\frac{F}{m} = C_F \frac{\rho_g u_{\text{rel}}^2}{\rho_l r} \quad ; \quad \frac{k}{m} = C_k \frac{\sigma}{\rho_l r^3} \quad ; \quad \frac{c}{m} = C_d \frac{\mu_l}{\mu_g r^2} \tag{4.20}$$

where $C_F = 1/3$, $C_k = 8$, $C_d = 5$ are constants, r the droplet radius, ρ the density, σ the surface tension, μ the viscosity, and the subscripts l and g indicate liquid and gases respectively.

The deformation x can be expressed by a non-dimensionless parameter y, hereafter referred as droplet distorsion, whose equivalence is $y = x/(C_b r)$, where $C_b = 0.5$ is a constant. Using the expressions from the Taylor analogy and introducing the change of variable y, the ODE (4.19) changes to:

$$\ddot{y} = \frac{C_F}{C_b} \frac{\rho_g}{\rho_l} \frac{u_{rel}^2}{r^2} - \frac{C_k \sigma}{\rho_l r^3} y - \frac{C_d \mu_l}{\rho_l r^2} \dot{y} \tag{4.21}$$

This expression governs the breakup of droplets, which will happen for $y > 1$ (i.e. when the amplitude of the oscillation x equals the radius of the undeformed droplet). For solving this equation, it is useful to introduce the following parameters:

$$t_d = \frac{2\rho_l r^2}{C_d \mu_l} \tag{4.22a}$$

$$\omega^2 = C_k \frac{\sigma}{\rho_l r^3} - \frac{1}{t_d^2} \tag{4.22b}$$

where t_d is the oscillation damping time and ω is the oscillations frequency. With these definition, the solution to Eq. (4.21) is:

$$y(t) = We_c + e^{-t/t_d} \left[(y_0 - We_c) \cos(\omega t) + \frac{1}{\omega} \left(\dot{y}_0 + \frac{y_0 - We_c}{t_d} \right) \sin(\omega t) \right] \tag{4.23}$$

where $We_c = \frac{C_F}{C_k C_b} We = We/12$ with the constants previously defined. The distorsion rate can be obtained by differentiating the former expression with time:

$$\dot{y}(t) = \frac{We_c - y(t)}{t_d} + e^{-t/t_d} \left[\left(\dot{y}_0 + \frac{y_0 - We_c}{t_d} \right) \cos(\omega t) - \omega (y_0 - We_c) \sin(\omega t) \right] \tag{4.24}$$

As it can be seen, the previous equations are continuous. For numerical implementation of the algorithm, it is more convenient to express them in their corresponding discrete form:

$$y^{n+1} = We_c + e^{-dt/t_d} \left[(y^n - We_c) \cos(\omega dt) + \frac{1}{\omega} \left(\dot{y}^n + \frac{y^n - We_c}{t_d} \right) \sin(\omega dt) \right] \tag{4.25}$$

$$\dot{y}^{n+1} = \frac{We_c - y^{n+1}}{t_d} + e^{-dt/t_d} \left[\left(\dot{y}^n + \frac{y^n - We_c}{t_d} \right) \cos(\omega dt) - \omega (y^n - We_c) \sin(\omega dt) \right] \tag{4.26}$$

where the subindexes n and $n+1$ indicate two consecutive time instants where dt is the timestep.

To estimate breakup, firstly ω^2 is calculated with Eq. (4.22b). According to its value, two options are present:

- If $\omega^2 < 0$, oscillations are not present. Hence, the droplet does not deform and the values for droplets distorsion and distorsion rate are set to 0: $y^{n+1} = y^n = 0$.

- If $\omega^2 > 0$, breakup is possible. In this case, the amplitude of oscillations A is calculated:

$$A = \sqrt{(y^n - We_c)^2 + (\dot{y}^n/\omega)^2} \tag{4.27}$$

Again, the value of A will present two different alternatives:

- If $We_c + A \leq 1$, then $y^n \leq 1$ and droplet will not break. Deformation and deformation rate will then be updated by applying Eqs. (4.25) and (4.26).

- If $We_c + A > 1$, breakup is possible. A breakup timestep dt_{bu} is then calculated as the smallest root of the following equation:

$$We_c + A\cos\left(\omega dt_{bu} + \phi\right) = 1 \qquad (4.28)$$

where the phase ϕ is obtained from the following:

$$\cos\phi = \frac{\dot{y}^n - We_c}{A} \quad ; \quad \sin\phi = -\frac{\dot{y}^n}{A\omega} \qquad (4.29)$$

Breakup will then occur in the case that $dt < dt_{bu}$, or also if updating the deformation it is found that $y^{n+1} > 1$. Once breakup is triggered, the associated droplet (named parent) will divide into one or several smaller particles (named children). The mean size of children droplets r_{32} is obtained through an energy balance between the produced droplets and the parent with radius r, yielding the following relation between both sizes:

$$\frac{r}{r_{32}} = 1 + \frac{8K}{20} + \frac{\rho_l r^3}{\sigma} \dot{y}^2 \left(\frac{6K - 5}{120}\right) \qquad (4.30)$$

where $K = 10/3$ is a constant. Now, radii of children droplets r_{ch} are randomly chosen from a Rosin-Rammler distribution [1] with characteristic diameter r_{32} and factor $q = 3.5$. Inverting Eq. (??) yields:

$$r_{ch} = r_{32}\sqrt[3.5]{-\log\left(1 - Q\right)} \qquad (4.31)$$

where Q is the value for the CDF. To sample droplets from this distribution, Q is sampled from a uniform distribution $\in [0,1]$. The resulting random number is introduced in the previous expression, yielding a value for one children droplet. This procedure is repeated until the volume of all children droplets equals the volume of the parent, hence conserving mass. Children droplets are then randomly located along the surface of the parent droplet. They will all inherit the velocity of the parent droplet, plus a component $v_\perp$ with magnitude:

$$v_\perp = C_v C_b r \dot{y}^n \qquad (4.32)$$

where $C_v \approx 1$. The direction of $v_\perp$ is randomly chosen in a plane normal to the relative velocity u_{rel}. Finally, all children droplets all initialised with $y = \dot{y} = 0$.

4.6.2 Enhanced TAB model

The main disadvantage of the TAB model is the underprediction of droplets size. To overcome this problem, an improved version of the TAB model was developed by **?**, named Enhanced Taylor-Analogy Breakup (ETAB). Breakup is predicted and triggered in the same way as in TAB, but the size of children droplet is estimated differently. While TAB makes use of an energy balance (**?**), ETAB considers that the droplet production rate is proportional to the number of children droplets. Mathematically, this proportionality is expressed by the following exponential decay law:

$$\frac{dm_{\mathrm{ch}}}{dt} = -3K_{\mathrm{br}} m_{\mathrm{ch}} \qquad (4.33)$$

where m_{ch} is the mass of children droplets. This law depends on the atomization regime through the breakup constant K_{br}, which depends on We and the oscillation frequency ω:

$$K_{br} = \begin{cases} k_1\omega & \text{if } We \leq We_t \\ k_2\omega\sqrt{We} & \text{if } We > We_t \end{cases} \qquad (4.34)$$

---

[1]In the original work by **?**, a χ^2 distribution is used

where k_1 and k_2 are constants, and We_t is a transition Weber number between bag and stripping breakup regimes, set to 80 (**?**). The bag breakup k_1 is obtained from the following expression to make a smooth transition between both regimes:

$$k_1 = k_1^* \left[\left(\frac{k_2}{k_1^*} \left(\sqrt{We_t} - 1 \right) \right) \left(\frac{We}{We_t} \right)^4 + 1 \right] \tag{4.35}$$

where $k_1^* = 2/9$. The stripping breakup constant is fixed to $k_2 = 2/9$.

The size of children droplets is calculated by integrating the production law Eq. (4.33):

$$\frac{r_{ch}}{r} = e^{-K_{br}t_{bu}} \tag{4.36}$$

where t_{bu} is estimated as in the TAB model, Eq. (4.28). All children droplets generated from a parent with radius r will have identical size r_{ch}. Finally, children will inherit parent's velocity plus a normal component given by:

$$v_\perp = C_A C_b r \left(\dot{y}^n \right)^2 \tag{4.37}$$

whose direction is randomly chosen in a plane normal to the relative velocity u_{rel}. In this expression, C_A is a constant determined from an energy balance:

$$C_A^2 = 3 \left(1 - \frac{r_{ch}}{r} + \frac{5}{72} C_D We \right) \frac{\omega^2}{\dot{y}^2} \tag{4.38}$$

being C_D is the drag coefficient of the parent droplet, Eq. (3.6). Note that $v_\perp$ defined by the ETAB model differs from TAB's Eq. (4.32) by considering C_A to be dependent on the breakup regime.

4.6.3 Gorokhovski stochastic model

Both TAB and ETAB models were derived using the Taylor analogy breakup. The TAB model is known to underdetermine the diameter of the children droplets and to not distinguish between breakup regimes, producing too many droplets when the Weber number is high. Hence, the applicability of TAB is restricted to breakup at low We. ETAB tried to solve this issue by considering an exponential decay law for the size of children droplets which would depend on the breakup regime. Both models are, however, deterministic in the sense that a single range of droplet sizes is considered when breakup is produced.

A different secondary atomization model not based on the Taylor analogy was derived by **?**. This model circumvents the deterministic approach of the TAB family of models by accounting for a range of children droplet sizes when breakup occurs. This is done by using a stochastic approach based on Kolmogorov's theory of breakup (**?**). Following this theory, the evolution of droplet's sizes is represented by a Fokker-Planck equation:

$$\frac{\partial T \left(\ln r, t \right)}{\partial t} = -\nu \langle \xi \rangle \frac{\partial T \left(\ln r, t \right)}{\partial \left(\ln r \right)} + \frac{1}{2} \nu \langle \xi^2 \rangle \frac{\partial^2 T \left(\ln r, t \right)}{\partial \left(\ln r \right)^2} \tag{4.39}$$

where $T \left(\ln r, t \right)$ is the cumulative distribution of droplets sizes, ν the breakup frequency, and $\langle \xi \rangle$ and $\langle \xi^2 \rangle$ are parameters. After some mathematical development (**?**), the cumulative distribution function can be expressed as:

$$T \left(\ln r, t \right) = \frac{1}{2} \left(1 + \text{erf} \left(\frac{\ln r - \ln r_{ch} - \langle \xi \rangle}{\sqrt{2 \langle \xi^2 \rangle}} \right) \right) \tag{4.40}$$

This function will be later used to obtain the size of children droplets. The previous step is to determine when breakup occurs. In this model, two criteria are used:

- Parent droplets must be larger than a critical radius r_{cr}. This value is determined from a critical Weber number $e_{\text{crit}} = 6$:

$$r_{\text{crit}} = \frac{We_{\text{crit}} \sigma}{\rho_g u_{\text{rel}}^2} \tag{4.41}$$

- The residence time of the particles must be larger than a computed breakup time t_{bu}:

$$t_{bu} = B\sqrt{\frac{\rho_l}{\rho_g}} \frac{r}{u_{rel}} \tag{4.42}$$

where $B = \sqrt{3}$.

If both $r > r_{\mathrm{crit}}$ and $t > t_{bu}$ (both criteria must be met) as given by the previous expressions, breakup occurs. In this case, size of children droplet is obtained from the cumulative density function $T(\ln r_{ch}, t)$, Eq. (4.40), from which lnr_{ch} can be solved:

$$\ln r_{ch} = \ln r + \langle\xi\rangle + \sqrt{2\langle\xi^2\rangle}\,\mathrm{erf}^{-1}(2T-1) \tag{4.43}$$

The size of children droplets are then obtained by sampling a random value of T from a uniform distribution between 0 and 1, and then applying the previous equation. The parameters $\langle\xi\rangle$ and $\langle\xi^2\rangle$ are the parameters of the model, and can be calculated from the following equations:

$$\langle\xi\rangle = K_1 \ln\left(\frac{We_c}{We}\right) \tag{4.44a}$$

$$-\frac{\langle\xi\rangle}{\langle\xi^2\rangle} = K_2 \ln\left(\frac{r}{r_{ch}}\right) \tag{4.44b}$$

where K_1 and K_2 are the constants of the model, which are of order unity. The constant K_1 controls the mean size of children droplets, while K_2 influences its standard deviation.

4.6.4   Analysis of sizes and number of children droplets

An analysis of sizes and estimated number of droplets produced by each model is done in the following lines.
The estimated number of children for each model can be obtained as:

$$N_{ch} = \left(\frac{r}{r_{ch}}\right)^3 \tag{4.45}$$

4.6.4.0.1   Gorokhovski   Constants K_1, K_2 need to be tuned. **2009 Apte** uses the values $K_1 = 0.6$ and $K_2 = 1$ for simulating spray in a swirl injector. **Senoner PhD 2010** uses $K_1 = 0.1$, $K_2 = 0.8$ for simulating a diesel spray injected in a high-pressure chamber; and the values $K_1 = 0.02$, $K_2 = 0.16$ for simulating a high-pressure jet in crossflow. The effect of these two constants will be investigated in our models.

As done for the models from the TAB family, a mean size for children droplets can be estimated. The parameter ξ from Eq. (4.40) is defined as $\xi = \ln\left(\frac{r_{ch}}{r}\right)$. Introducing this expression into Eq. (4.44a)

$$\langle\ln\left(\frac{r_{ch}}{r}\right)\rangle = K_1 \ln\left(\frac{We_c}{We}\right) \tag{4.46}$$

By rearranging this equation we can express the mean size of children droplets:

$$\langle\frac{r_{ch}}{r}\rangle = \left(\frac{We_c}{We}\right)^{K_1} \tag{4.47}$$

This equation confirms the previous statement that the constant K_1 has a direct influence on the size of children droplet generated: the larger K_1 is, the smaller children droplets are (since the ratio $We_c/We < 1$). Generated children droplet can still undergo further breakup if they meet the breakup conditions (cascade effect), so decreasing K_1 would a priori limit the size of droplets (and hence their number) only in each iteration. Nevertheless, this can suppose a smooth transition of breakup towards equilibrium, which would ensure that the Weber number of children droplets is closer to its critical value (i.e. the limit of breakup). An aggressive breakup, which could be produced with a low value of K_1, could generate many children droplets from a parent particle with very small size that would not be found in reality (see Figures 4.9 and 4.11).
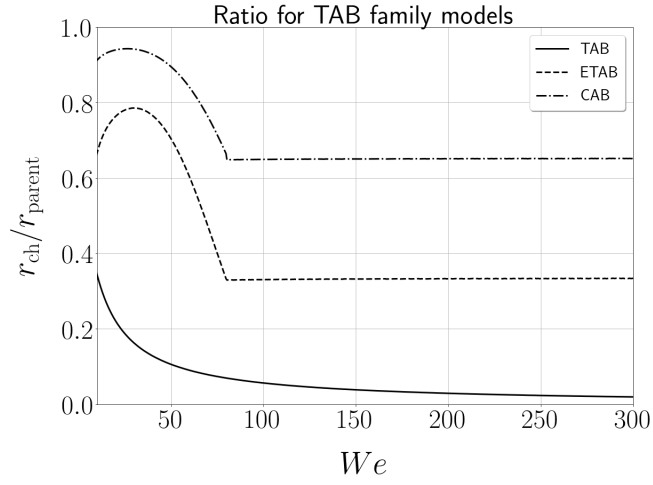
Figure 4.8: Ratio of mean droplet for TAB family of models
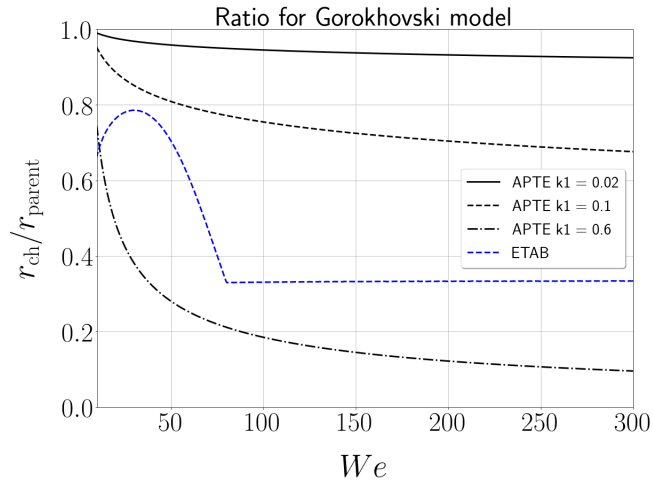

Figure 4.9: Ratio of mean droplet for Gorokhovski model
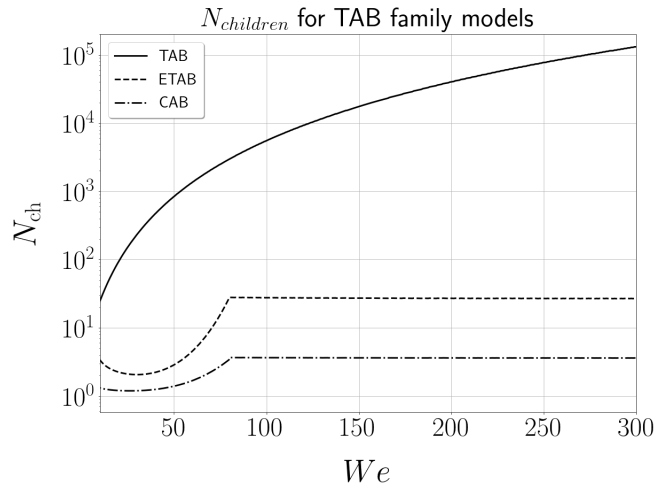

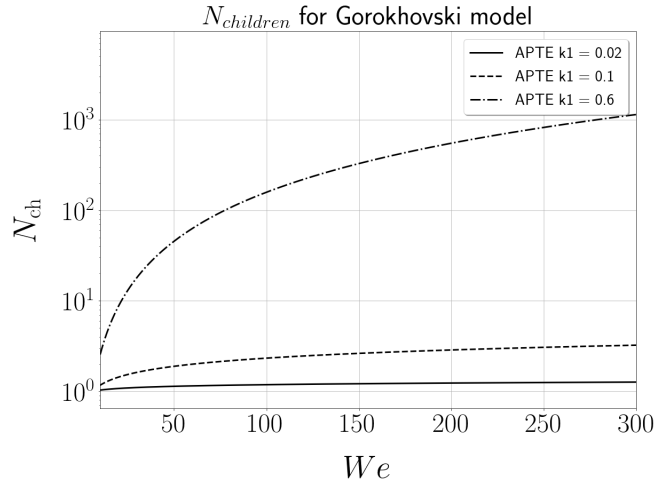Figure 4.10: Estimated number of children for TAB family of models

Figure 4.11: Estimated number of children for Gorokhovski model

4.7 Subgrid models for turbulent dispersion

Review

Regarding turbulent dispersion models, there are the ones used in RANS studies:

- **2016 Eckel** mentions two dispersion models: Gosmann and Ioannides (the classic) (1983), (Blumcke et al. 1993)

- **Fontes 2018** uses the Langevin dispersion model introduced in Sommerfeld 2001

- **Belmar 2020** presents a turbulent dispersion model by O'Rourke.

For LES, Iafrate 2016 shows a good modelling of turbulent dispersion applied to gasoline injection (§8.2 Impact de la turbulence sous-maille), based on references 120-124.
    Also, references I have for LES are 2015 Minier, Minier ref. 57, 2014 Urzay - Particle-laden flows.
    A nice one is the techical report Amsden 1989 - KIVA II.
    OJO: reference OKongo and Bellan de Minier ref. 57 puede ser fundamental, hace analisis de particulas con distintas velocidades inyectadas !!

4.8 Conclusions

This chapter has presented the methodology
    For further development of the models, the following perspectives are proposed:

- In the **lagrangian injectors learning** part, the deformation of the liquid structures sampled in resolved atomization simulations could be considered to impose a modified drag coefficient in the dispershed phase simulations. This would allow for a more accurate transport of the lagrangian spray, specially at the first time instants of injection before secondary breakup takes place. Also, the transient spray obtained through the accumulation process can be considered to develop an unsteady injection model, which could be useful in reactive cases where thermoacoustic oscillations take place, such as gas turbine and rocket engines. The convergence criterion, defined as a MSE norm on the droplet diameters, could be extended to include other parameters such as liquid velocities and mass flow rates.

Chapter 5

Learning data from a resolved liquid jet in crossflow

Describe here all our simulations done with JICF, what we have achieved with them, etc.

- Experimental setup description

- Numerical setup description. Operating points

- Mesh convergence study

- Spray sampling

- Direct measurement of fluxes with interior boundaries

- Liquid disappearing (set levelset band) ??

- Results:

  - Breakup mechanisms

  - In-nozzle phenomena of flow separation (and entrainment of gaseous bubbles)

  - Spray formation and evolution with axial distance

- Other results:

  - Slip velocity evolution

  - Vorticity distribution (horse-shoe vortices, double vortical structural in liquid)

5.1 Introduction

5.2 Experimental test case

5.3 Computational setup

Numerical domain

Operating conditions

5.4 Results

5.4.1 Validation with experimental trajectory

5.4.2 Jet topology and breakup

5.4.2.1 Effect of mesh

5.4.2.2 Effect of operating point

5.4.3 Spray characterization

5.4.3.1 Sampling procedure for droplets

5.4.3.2 Droplets size distributions

5.4.3.3 Direct measurement of fluxes (interior boundaries)

5.4.4 Dense core effect and characterization

5.4.5 Mass conservation in ACLS

5.4.6 Computational performances

5.4.7 Spatial discretization of sprays

5.5 Conclusions

Chapter 6

Validation in liquid jet in crossflow

Describe here all our results from the lagrangian simulations:

- Effects of applying full workflow: w/wo ALM, w/wo secondary atomization ...

- Mesh convergence study: specify it

- Validation with experiments

- Mass conservation issues: lagrangian tracking, etc.

6.1   Introduction

6.2   Models sensitivity

ALSO: effect of one and two-way coupling !! Ver articulos 2010, 2011 Li

6.2.1   Effect of injection conditions

6.2.2   Effect of secondary atomization model

6.2.3   Effect of dense core blockage effect model

6.3   Results

6.3.1   Mesh convergence study

6.3.2   Validation with experiments (quantitative/qualitative)

6.4   Conclusions

Part III

Application to a multipoint injector

Chapter 7

Gaseous flow in BIMER multipoint injector

7.1 Introduction

The jet in crossflow atomizer from the previous chapters is an academic test case of fuel representative of LPP systems. Its study is of interest for aeronautical gas turbines since it uses kerosene as injected liquid and it has been tested in a high-pressure environment. Yet, its

The fact that the injected liquid is kerosene is

Here we describe the aerodynamic simulations performed with BIMER. Two operating points are simulated:

7.2 Experimental setup

Dodecane properties are shown in Table 7.1

Table 7.1: Physical properties of dodecane fuel.

ρ [kg m^{-3}]	μ [Pa s]	σ [N/m]
750	$1.36 \cdot 10^{-3}$	$22 \cdot 10^{-3}$

7.3 Choice of operating points

In first place, the

Gaseous flow simulations of BIMER have been performed for two operating conditions tested experimentally, with the purpose of using one condition for validation and the other for application:

- **Validation** of the gaseous simulations is performed with the operating point tested experimentally by **?**, since this one presents data on the non-reactive aerodynamic field. The simulations are also compared to numerical results obtained for this same operating condition by **?**.

- **Application** to the setup condition tested by **?**. This study shows data on non-reactive spray characteristics, and hence it will be used as the application case to run the full workflow formerly introduced in Chapter 4. It is, however, not used for validating the gaseous simulations since it does not present pertinent data.

Both ope

Table 7.2: Operating points for performing non-reactive gaseous simulations

Operating condition	$\dot{m}_g$ [g s^{-1}]	T_g [K]	ρ_g [kg m^{-3}]	μ_g [Pa s]	p [Pa]
Validation (?)	53	473	0.746089	$2.571 \cdot 10^{-5}$	101300
Application (?)	43.1	433	0.816382	$2.3911 \cdot 10^{-5}$	101300

Table 7.3: BIMER operating point to validate non-reactive gaseous simulations tested by ?

$\dot{m}_g$ [g s^{-1}]	T_g [K]	ρ_g [kg m^{-3}]	μ_g [Pa s]	p [Pa]
53	473	0.746089	$2.571 \cdot 10^{-5}$	101300

7.4 Numerical setup

7.5 Validation of gaseous field

Show nice streamlines (Fig. 6.4 Esclapez-1) and PVC. It would be nice to compare them for both operating conditions

7.6 Application point

7.7 Conclusion

Chapter 8

Spray learning from resolved atomization simulations of BIMER

8.1 Introduction

8.2 Numerical setup

Table 8.1: Operating point to perform gaseous and two-phase simulations tested by **?**

Air properties			
$\dot{m}_g$ [g s^{-1}]	T_g [K]	ρ_g [kg m^{-3}]	μ_g [Pa s]
43.1	433	0.816382	$2.3911 \cdot 10^{-5}$
Liquid properties			
$\dot{m}_l$ [g s^{-1}]	ρ_l [kg m^{-3}]	μ_l [Pa s]	σ [N/m]
1.64	750	$1.36 \cdot 10^{-3}$	$22 \cdot 10^{-3}$
Burner staging			
α [%]	$\dot{m}_{l,pilot}$	$\dot{m}_{l,takeoff}$	
15	0.25	1.39	

8.3 Liquid injection through one multipoint hole

8.4 Injectors learning

8.5 Conclusion

Chapter 9

Applicaton to dispersed phase simulations in BIMER

9.1 Introduction

9.2 Injector definition for resolved atomization hole

9.3 Extrapolation of injectors to rest of multipoint holes

The

9.3.1 Injectors geometry

$$\boldsymbol{x}_0 = \begin{pmatrix} -38.5 \text{ mm} \\ r \cos \alpha_0 \\ r \sin \alpha_0 \end{pmatrix} \tag{9.1}$$

$$\boldsymbol{x}_i = \begin{pmatrix} -38.5 \text{ mm} \\ r \cos \alpha_i \\ r \sin \alpha_i \end{pmatrix} \tag{9.2}$$

9.3.2 General procedure

1. Obtain parameters for SLI of injector 0 (baseline parameters):

$$\alpha_0 \ ; \ \boldsymbol{n}_0 \ ; \ \theta_0 = 90 - \alpha_0 - atan\left(\frac{n_y}{n_z}\right) \ ; \tag{9.3}$$

2. Get parameters for SLI of injector i from baseline:

$$\alpha_i = \alpha_0 - i\Delta\alpha \tag{9.4}$$

$$\boldsymbol{n}_i = \tag{9.5}$$

$$\theta_1 = \theta_0 \tag{9.6}$$

9.3.3 Definition of coordinate systems and operations

The global coordinate system is:

$$\boldsymbol{x} = \begin{pmatrix} x \\ y \\ z \end{pmatrix} \tag{9.7}$$

The local (crossflow) coordinate system is:

$$\boldsymbol{x}^{cr} = \begin{pmatrix} x^c \\ y^c \\ z^c \end{pmatrix} \tag{9.8}$$

with the following equivalences between local and global systems :

$$\boldsymbol{x}^c = \boldsymbol{n} \quad ; \quad \boldsymbol{z}^c = \boldsymbol{x} \quad ; \quad \boldsymbol{y}^c = \boldsymbol{z}^c \times \boldsymbol{x}^c \tag{9.9}$$

where the rotation matrix being:

$$\boldsymbol{R} = \begin{pmatrix} \boldsymbol{x}^{c^T} \\ \boldsymbol{y}^{c^T} \\ \boldsymbol{x}^{c^T} \end{pmatrix} \tag{9.10}$$

More elegantly expresses:

$$\boldsymbol{R} = \begin{pmatrix} x_x^c & x_y^c & x_z^c \\ y_x^c & y_y^c & y_z^c \\ z_x^c & z_y^c & z_z^c \end{pmatrix} \tag{9.11}$$

Transformation for droplet locations is translation + rotation

$$\boldsymbol{x}_{\mathrm{dr}}^c = \boldsymbol{R}\left(\boldsymbol{x}_{\mathrm{dr}} - \boldsymbol{x}_0\right) \tag{9.12}$$

For droplet velocities, transformation is only rotation:

$$\boldsymbol{u}_{\mathrm{dr}}^c = \boldsymbol{R}\boldsymbol{u}_{\mathrm{dr}} \tag{9.13}$$

Inverse transform then:

$$\boldsymbol{x}_{\mathrm{inj}} = \boldsymbol{x}_0 + \boldsymbol{R}^{-1}\boldsymbol{x}_{\mathrm{inj}}^c \tag{9.14}$$

$$\boldsymbol{u}_{\mathrm{inj}} = \boldsymbol{R}^{-1}\boldsymbol{u}_{\mathrm{inj}}^c \tag{9.15}$$

9.4 Conclusion